ACS APPLIED NANO MATERIALS

www.acsanm.org

Article

Superior Multifunctional Nickel Ferrite Nanoparticles and Graphite-Integrated Thermoplastic Polyurethane Nanocomposites for Electromagnetic Interference Shielding, Joule Heating, and Photothermal Applications

Anju, Milan Masař, Michal Machovský, Michal Urbánek, Pavol Šuly, Jiří Matyáš, Jarmila Vilčáková, Ivo Kuřitka, and Raghvendra Singh Yadav*

Cite This: *ACS Appl. Nano Mater.* 2026, 9, 353−369

Read Online

ACCESS | Metrics & More | Article Recommendations | Supporting Information

ABSTRACT: The introduction of next-generation electronic devices, multimedia communication, and the miniaturization of the electronics industry has emphasized the need for the development of lightweight electromagnetic interference (EMI) shielding materials. Herein, we fabricated thermoplastic polyurethane (TPU)-based nanocomposites incorporated with conducting filler graphite (G) and magnetic filler nickel ferrite (NF) nanoparticles using the melt-mixing approach with varying amounts of conducting and magnetic filler. The developed G40NF5@TPU nanocomposite, comprising 40 wt % graphite and 5 wt % $NiFe_2O_4$ nanoparticles, exhibited superior EMI shielding performance with a total EMI shielding effectiveness of 41.6 dB, capable of blocking 99.99% of incident radiation in the 8.2−12.4 GHz frequency range at a thickness of only 1.95 mm. To elucidate the mechanisms contributing to the high shielding performance, various factors were analyzed, highlighting the roles of high dielectric, magnetic, and conduction losses in achieving superior attenuation. Beyond EMI shielding, the G40NF5@TPU nanocomposite exhibited a remarkable, stable, and durable electrothermal conversion response, with a surface temperature reaching up to ∼154 °C at a low driving voltage of 7 V. The developed G40NF5@TPU nanocomposites also exhibited a stable photothermal response, achieving surface temperatures of up to ∼37 °C under mild solar-simulated irradiation. The synergistic combination of superior EMI shielding performance, efficient electrothermal and photothermal conversion capabilities, and hydrophobicity highlights the remarkable versatility of the G40NF5@TPU nanocomposite. Owing to these combined features, G40NF5@TPU emerges as a highly promising candidate for next-generation electronic and communication devices, personal thermal management devices, defense and aerospace components, and other advanced technologies that require both robust EMI protection and efficient thermal regulation in harsh or variable environments.

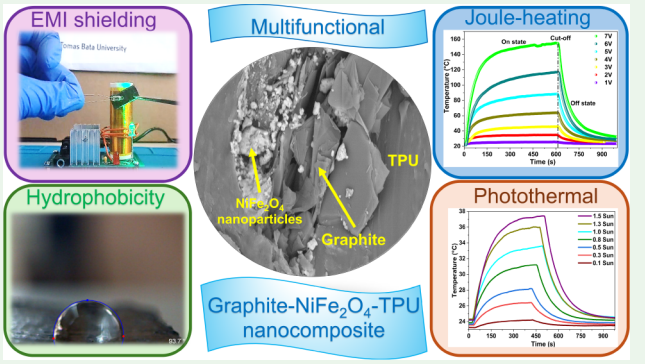

KEYWORDS: *EMI shielding, polymer nanocomposites, TPU, nickel ferrite, graphite*

1. INTRODUCTION

Over time, the need for intelligent electronic equipment, ranging from communication devices to wireless networks, has significantly boosted.[1] With the rapid advancement in next-generation high-speed information technology, the integration of electronic devices and the introduction of artificial intelligence have intensified electromagnetic interference (EMI) as a potential threat.[1] EMI not only disrupts device functionality but also poses risks to biological processes in humans.[2] There is a growing demand for high-performance EMI shielding materials to mitigate the adverse effects of electromagnetic (EM) waves on electronic and communication devices. Moreover, electronic devices operating in harsh or extremely cold environments often suffer from performance degradation or even complete failure. Consequently, the development of multifunctional materials that combine efficient EMI shielding with on-demand thermal management is essential to ensuring the stable operation of electronic devices in challenging environments. EMI shielding materials with Joule heating and photothermal conversion can ensure the reliability of these devices under such conditions. Materials capable of photothermal conversion offer heating under solar

Received: October 8, 2025
Revised: December 1, 2025
Accepted: December 15, 2025
Published: December 22, 2025

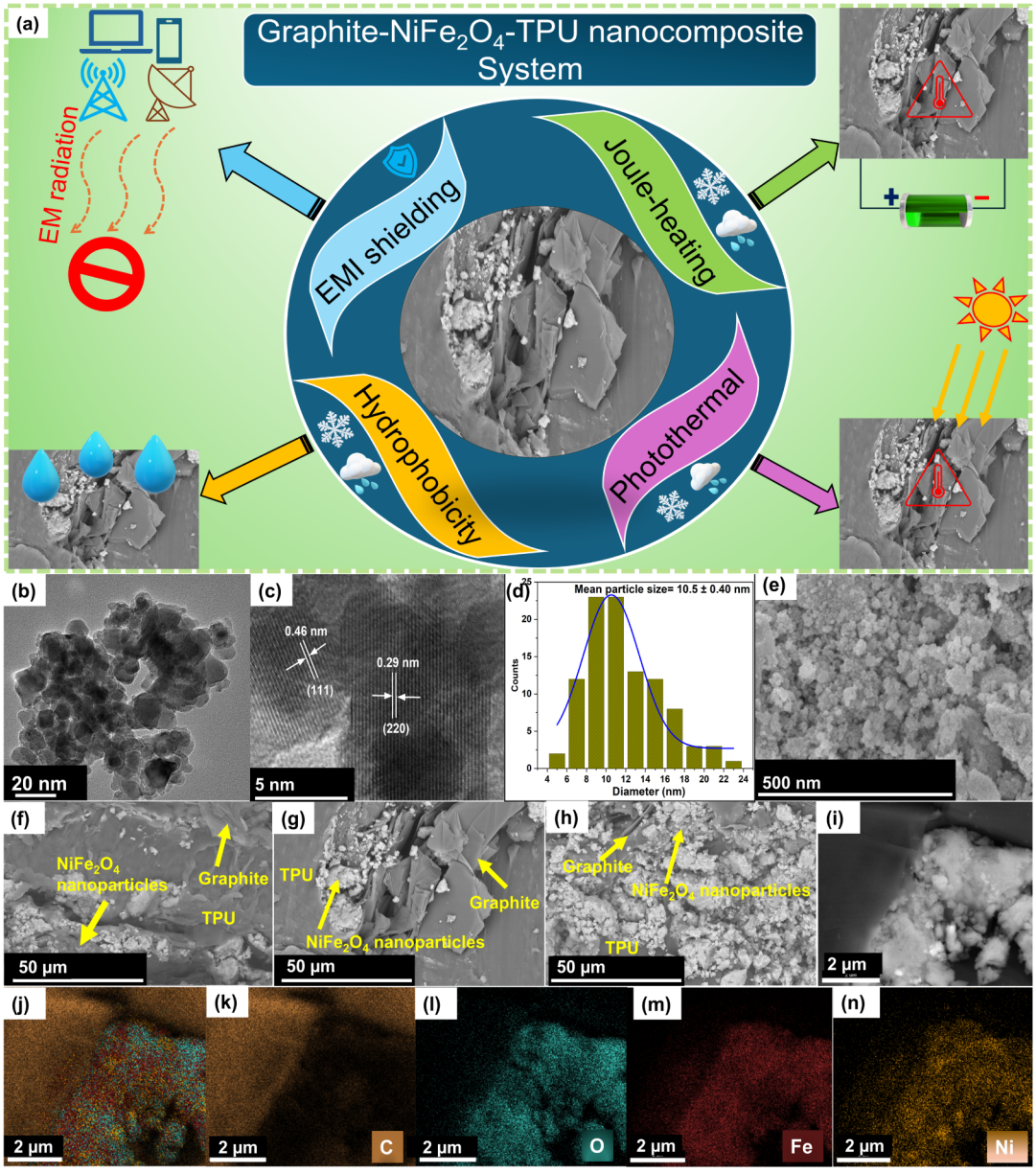

Figure 1. (a) Illustration of the G40NF5@TPU nanocomposite system and its applications, (b) TEM, (c) HRTEM image of $NiFe_2O_4$ nanoparticles, (d) particle size distribution, (e) FE-SEM of $NiFe_2O_4$ nanoparticles, (f) FE-SEM of G40NF5@TPU, (g) FE-SEM of G35NF10@TPU, (h) FE-SEM of G30NF15@TPU nanocomposites, (i–n) FE-SEM and Elemental mapping of the G40NF5@TPU nanocomposite.

irradiation, thus addressing both energy efficiency and environmental pollution concerns.[3]

Recently, polymers filled with various fillers have emerged as promising materials for multifunctional applications.[4,5] Thermoplastic polyurethane (TPU) is known for its excellent mechanical properties and flexibility, rubber-like elasticity, making it ideal for producing flexible polymer composites.[6] However, its poor EMI shielding properties limit its broader application in this area. The material characteristics of the TPU matrix make it very suitable for integration into composite formulations. TPU, when combined with electrically conductive and magnetic fillers, offers synergistic dielectric and magnetic losses, resulting in balanced impedance matching that enhances the absorption of EM waves rather than relying on reflection-based shielding. The electrically conductive nanofillers provide superior electrical conductivity for EMI shielding and improved EMI shielding owing to their nanostructure and composition. Fillers with a high aspect ratio or surface area are especially useful for establishing a conductive pathway within the polymer. In addition, filler selection and loading weight percentage are essential in determining the EMI shielding characteristics of the polymer nanocomposites. Indeed, a high filler loading concentration can significantly enhance the characteristics of the polymer nanocomposites. However, loading large amounts of fillers presents challenges such as uniform dispersion, discontinuous linked chains, agglomeration, poor mechanical characteristics, etc.[7] Previously, a research group, Ma et al.[8] designed silver-coated and foamed temperature-sensitive microsphere FTSM/Fe_3O_4/waterborne polyurethane (WPU) composite aerogels and demonstrated an EMI SE of 46.5 dB. Further, Liu et al.[9] prepared graphene@$NiFe_2O_4$ films on a polyimide substrate and reported EMI shielding performance, with a total EMI SE reaching up to 51 dB. Previously, in our research group Anju et al.[10] also

https://doi.org/10.1021/acsanm.5c04619
ACS Appl. Nano Mater. 2026, 9, 353−369

developed cobalt ferrite-graphite-TPU nanocomposites and demonstrated an efficient EMI SE of 41.5 dB at a thickness of 5 mm. However, a change in the magnetic filler type and synthesis pathway can strongly influence particle morphology, dispersion, and magnetic interactions within the TPU matrix and further can provide efficient EMI shielding characteristics of polymer nanocomposites at lower thickness. The anisotropy energy is higher for nanocomposites having spinel ferrite of moderate saturation magnetization.[11] Higher anisotropy energy can improve EM wave absorption at higher frequencies.[12] Due to moderate saturation magnetization, high Curie temperature, large permeability, and high magnetic losses over other ferrites, $NiFe_2O_4$ nanoparticles were chosen as a magnetic filler in the TPU matrix. $NiFe_2O_4$ nanoparticles were synthesized using a simple one-pot sol−gel autocombustion method. Graphite is preferred as a conductive filler because of its low cost and electrically conductive nature. The novelty of this research work lies in the design and fabrication of TPU-based polymer nanocomposites using a melt-mixing approach, incorporating $NiFe_2O_4$ nanoparticles and graphite as fillers. Furthermore, the developed G40NF5@TPU polymer nanocomposite exhibited superior EMI shielding characteristics at a lower thickness of only 1.95 mm and at a lower total filler content (45 wt %), demonstrating improved shielding efficiency at lighter weight and smaller dimensions. Notably, the optimization behavior of $NiFe_2O_4$-based systems contrasts with $CoFe_2O_4$-based systems, with maximum performance observed at 5 wt % $NiFe_2O_4$ nanoparticles and 40 wt % graphite. In addition to quantitative EMI shielding measurements, the shielding performance of the G40NF5@TPU nanocomposite was visually demonstrated and verified by using a Tesla coil, providing clear experimental evidence of its effectiveness. Beyond EMI shielding, the developed G40NF5@TPU nanocomposite demonstrated multifunctional applications (Figure 1a), including an outstanding and stable Joule heating response with a surface temperature reaching up to ∼154 °C at a low driven voltage, and a stable, efficient, and repeatable photothermal response, with a surface temperature of ∼37 °C under mild simulated solar irradiation. In addition, the improved hydrophobic property of the developed G40NF5@TPU nanocomposite makes it suitable for use in moisture-rich environments.

To the best of our knowledge, this is the first comprehensive study on $NiFe_2O_4$-graphite@TPU nanocomposites that combines superior EMI shielding at reduced thickness with multifunctional properties such as photothermal conversion, Joule heating, and moisture resistance.

2. EXPERIMENTAL SECTION

2.1. Chemicals. Iron(III) nitrate nonahydrate ($Fe(NO_3)_3{\cdot}9H_2O$) and nickel(II) nitrate hexahydrate ($Ni(NO_3)_2{\cdot}6H_2O$) were obtained from Alfa Aesar GmbH & Co KG, Germany. Soluble starch ($(C_6H_{10}O_5)_n$) derived from potatoes was sourced from Lach-Ner, Czech Republic, while graphite was purchased from Sigma-Aldrich, Germany. A TPU Elastollan 1195A was used as a polymer matrix.

2.2. Synthesis of $NiFe_2O_4$ Nanoparticles. $NiFe_2O_4$ nanoparticles were synthesized using a starch-mediated sol−gel autocombustion method, as demonstrated in Scheme S1 in the Supporting Information file. In the first step, measured quantities of nickel nitrate and iron nitrate were dissolved in deionized water with continuous stirring to produce a homogeneous solution. A separate solution of starch in deionized water was then prepared and slowly added to the metal salt mixture with stirring maintained. This combined mixture was heated at 100 °C, resulting in the formation of a gel as the water evaporated. Once the gel had formed, it was further heated to 300 °C, during which a spontaneous combustion reaction occurred. After being cooled, the resulting product was finely ground using a mortar and pestle, finally $NiFe_2O_4$ nanoparticles in powdered form were obtained.

2.3. Development of GNF@TPU Nanocomposites. The schematic representation of the $NiFe_2O_4$ nanoparticles-graphite-TPU nanocomposite, prepared using a melt-mixing approach, is illustrated in Scheme S1 in the Supporting Information file. Pure TPU granules were predried overnight at a temperature of 95 °C before melt-processing. TPU polymer nanocomposites embedded with $NiFe_2O_4$ nanoparticles and graphite were fabricated utilizing a melt-mixing process at 190 °C. The developed TPU nanocomposites were compressed and molded into a sheet with a uniform thickness of 1.95 mm, maintaining a total filler content of 45 wt %. Three sets of rectangular-shaped TPU-based nanocomposites, each with a thickness of 1.95 mm, were fabricated with varying weight percentages of $NiFe_2O_4$ nanoparticles and graphite, as detailed in Table S1 in the Supporting Information file.

3. CHARACTERIZATION

The morphology of $NiFe_2O_4$ nanoparticles was assessed by Transmission Electron Microscopy (TEM) and High-Resolution TEM (HR-TEM) with a JEM-2100Plus instrument (Jeol, Tokyo, Japan). To further investigate the fractured surface of the developed polymer nanocomposites, Field-Emission Scanning Electron Microscopy (FE-SEM) was employed, utilizing an FEI NanoSEM 450 (FEI Company, The Netherlands). Energy-dispersive X-ray spectroscopy (EDX) analysis was done to evaluate the composition of the developed polymer nanocomposite. The crystal structures of both the fillers (graphite and $NiFe_2O_4$ nanoparticles) and the GNF@TPU polymer nanocomposites were analyzed using X-ray diffraction (XRD) patterns acquired with a Rigaku MiniFlex 600 X-ray diffractometer (Rigaku Corporation, Tokyo, Japan). Furthermore, the magnetic properties of the synthesized $NiFe_2O_4$ nanoparticles and the GNF@TPU polymer nanocomposites were examined using a Model 7404, Lake Shore, Westerville, OH vibrating sample magnetometer (VSM). Thermogravimetric Analysis (TGA) and Differential Thermogravimetric Analysis (DTG) were conducted using a Setaram LabSys Evo equipped with a TG/DSC sensor in a nitrogen environment, covering a temperature range from 25 to 1000 °C at a heating rate of 10 °C min^{-1}. The surface wettability of the pristine TPU and the G40NF5@TPU nanocomposite was evaluated by measuring the water contact angle (WCA) using the SEE System (Advex Instruments, Czech Republic). The tensile behavior of neat TPU and the G40NF5@TPU nanocomposite was analyzed using a universal testing machine (Model M350-5CT) manufactured by Testometric Co., Ltd., Rochdale, UK. Rectangular-shaped TPU-based nanocomposites were employed in a WR90 waveguide to assess the scattering parameters using a PNA-L network analyzer (Agilent N5230A) within the frequency range of 8.2 to 12.4 GHz. Three samples from each developed nanocomposite sheet were cut and measured to obtain an average EMI SE value for precision. Complex permittivity and complex permeability were evaluated using the integrated Nicolson−Ross−Weir technique from the PNA-L network analyzer (Agilent N5230A) over the frequency range of 8.2 to 12.4 GHz. The reflectance spectra were measured using a Lambda 1050 UV−vis−NIR spectrometer (PerkinElmer systems) equipped with the integrating sphere accessory (250−2500 nm). The photothermal response was measured by irradiating the developed polymer nanocomposite using the

https://doi.org/10.1021/acsanm.5c04619
ACS Appl. Nano Mater. 2026, 9, 353−369

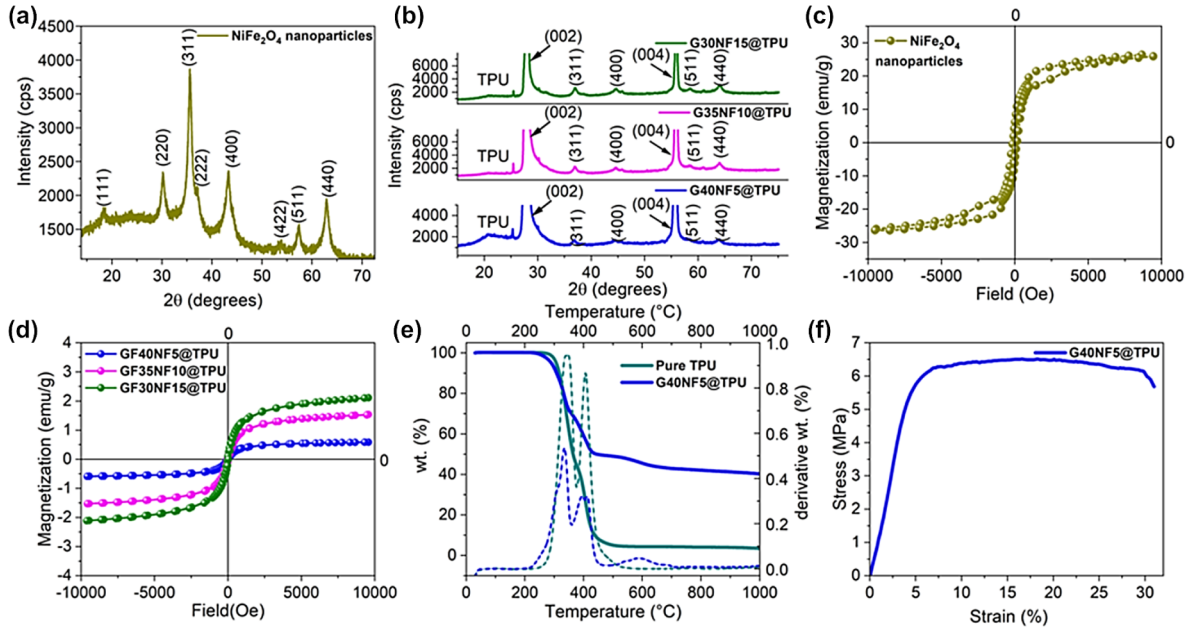

Figure 2. (a) XRD of $NiFe_2O_4$ nanoparticles, (b) magnified view of the XRD of developed GNF@TPU nanocomposites. (c) M-H curve of $NiFe_2O_4$ nanoparticles. (d) M-H curve of developed GNF@TPU nanocomposites. (e) TGA and DTG curve of Pure TPU and the G40NF5@TPU nanocomposite. (f) Stress−strain curve of the G40NF5@TPU nanocomposite.

Pico Solar Simulator KLMNO (parameters: illumination Spectrum: 350−1450 nm, working Distance: 3 cm, illumination Spot: 9 cm^2) AM1.5G spectral distribution with variable irradiance intensity (10−150%, or 0.1−1.5 Sun) where 1 Sun corresponds to (87.5 ± 4.3) mW cm^{-2}. A K-type thermocouple was connected to the developed nanocomposite sample to measure the sample's temperature response over time, and a data logger was used to collect the data. To avoid direct heating of the thermocouple by the incident light, it was connected to the sample from the bottom side. The Joule heating performance was investigated by connecting the developed polymer nanocomposite to an HMC 8043 power source (Rohde & Schwarz GmbH & Co. KG) at a constant voltage. A UT71C multimeter (UNI-TREND TECHNOLOGY (CHINA) CO., Ltd.) was used to measure the temperature. A thermocouple for temperature measurement was connected to the multimeter. Temperature was measured simultaneously with time. The surface temperature of the developed nanocomposite was measured using a FLIR E5-XT Wi-Fi thermal camera with a 160 × 120-pixel resolution.

4. RESULTS AND DISCUSSION

4.1. Microstructure and Morphology Study. TEM microscopy of $NiFe_2O_4$ nanoparticles confirmed spherical nanoparticles, as shown in Figure 1b. The HRTEM image in Figure 1c displayed interplanar spacings of 0.46 and 0.29 nm, which is attributed to the (111) and (220) crystal lattice planes, respectively.[13] Furthermore, the particle size distribution, shown in Figure 1d, shows that the particle sizes of the $NiFe_2O_4$ nanoparticles range from 4 to 24 nm, with an average particle size of 10.5 nm. Figure 1e illustrates the FE-SEM micrograph of $NiFe_2O_4$ nanoparticles, revealing that their morphology is predominantly spherical and of a regular shape. In addition, the microstructures of all developed polymer nanocomposites were also investigated and are illustrated in Figure 1f−h. The presence of $NiFe_2O_4$ nanoparticles was observed in all of the developed polymer nanocomposites, along with graphite in the TPU matrix, indicating their successful incorporation. Furthermore, the elemental mapping analysis of the G40NF5@TPU nanocomposite, depicted in Figure 1i−n, confirms the presence and spatial distribution of nickel (Ni), iron (Fe), oxygen (O), and carbon. $NiFe_2O_4$ nanoparticles and graphite fillers were evenly distributed, resulting in a good dispersion in the nanocomposite structure, which can enhance multiple interfacial interactions between graphite, $NiFe_2O_4$ nanoparticles, and the TPU matrix.[4] Enhanced interfacial polarization can help improve EM wave absorption in the developed G40NF5@TPU nanocomposite. An energy-dispersive X-ray study of the developed G40NF5@TPU nanocomposite was conducted, as shown in Figure S1 of the Supporting Information file. The EDAX spectrum confirmed the existence of nickel (Ni), iron (Fe), oxygen (O), and carbon (C) in the G40NF5@TPU nanocomposite.

4.2. Structural Analysis. To investigate the crystal structure, an XRD study of $NiFe_2O_4$ nanoparticles was carried out, as demonstrated in Figure 2a. The synthesized $NiFe_2O_4$ nanoparticles presented distinct peaks at 18.5°, 30.2°, 35.6°, 36.9°, 43.2°, 53.7°, 57.3°, and 62.9°. These peaks are associated with the (111), (220), (311), (222), (400), (422), (511), and (440) Bragg reflection planes, confirming the successful formation of $NiFe_2O_4$ nanoparticles.[14] The crystallite size was determined using the well- known Scherrer's equation as given below:

$$D = \frac{k\lambda}{\beta \cos\theta}$$

where D refers to crystallite size, k is the shape factor, λ denotes the X-ray wavelength, θ refers to the Bragg angle in degrees, and β is the full width at half maxima measured in radians. The crystallite size of the $NiFe_2O_4$ nanoparticles was determined to be 9.47 nm, as calculated from the most intense peak corresponding to the (311) diffraction plane.

Furthermore, Figure 2b demonstrates magnified XRD patterns for the developed GNF@TPU nanocomposites. The

https://doi.org/10.1021/acsanm.5c04619
ACS Appl. Nano Mater. 2026, 9, 353−369

XRD peaks corresponding to the graphite fillers can be observed at 27.8° and 55.7°, corresponding to the (002) and (004) diffraction planes, respectively.[15] Furthermore, the existence of $NiFe_2O_4$ nanoparticles was confirmed in the magnified view of the XRD patterns for the generated GNF@TPU nanocomposites, indicating that both fillers were successfully incorporated into the polymer matrix. Additionally, a broad diffraction peak extending from 20° to 25.2° confirmed the existence of TPU along with both fillers.[16,17]

4.3. Magnetic Characteristics. The M-H curve of the $NiFe_2O_4$ nanoparticles depicted in Figure 2c confirmed the ferromagnetic behavior of the $NiFe_2O_4$ nanoparticles with a saturation magnetization M_s value of 26 emu/g. The remanent magnetization (M_r) was measured to be 5.1 emu/g, while the coercivity (H_c) was found to be 135.6 Oe. Furthermore, Figure 2d illustrates the M-H curves of the prepared GNF@TPU polymer nanocomposites. As anticipated, the saturation magnetization value of the developed polymer nanocomposites was noticed to have significantly dropped compared with the saturation magnetization value of $NiFe_2O_4$ nanoparticles. This reduction can be attributed to the incorporation of $NiFe_2O_4$ nanoparticles into the nonmagnetic polymer matrix along with a secondary nonmagnetic filler. However, with an increasing wt % of $NiFe_2O_4$ nanoparticles, a monotonic enhancement in the magnetization was also noticed. The evaluation of saturation magnetization, coercivity, and remanent magnetization has been conducted for the developed GNF@TPU nanocomposites and is summarized in Table S2 of the Supporting Information file.

4.4. Thermal Stability. A thermal stability study was conducted under a N_2 atmosphere to investigate the stability of the developed polymer nanocomposites. The TGA and DTG curves of pure TPU and the developed G40NF5@TPU polymer nanocomposite are demonstrated in Figure 2e. As can be seen, the first-stage degradation is initiated at approximately 285 °C for pure TPU. Segmented polyurethanes generally degrade at different temperatures for hard and soft segments.[18] Hard domains degrade at lower temperatures, while soft segments of TPU degrade at slightly higher temperatures. Initially, the urethane bond of the hard segments in TPU is degraded, followed by the thermal degradation of the soft segments at around 376 °C. Above 500 °C, no further mass loss is observed, demonstrating the destruction of the polymer, leaving only 0.78% of char. After the inclusion of fillers in the developed G40NF5@TPU nanocomposite, the onset temperature was recorded at 260 °C. The lower degradation onset temperature can be associated with the thermal and mechanical stress applied to the polymer matrix during the melt-mixing process. On the other hand, the two main degradation steps correspond to the degradation of the TPU matrix, being completed below 500 °C. Interestingly, for the developed G40NF5@TPU nanocomposite, the last degradation step was observed at 592 °C, followed by a flat, minimal slope, mass decrease up to the maximum temperature. This can be attributed to the final step of thermal degradation observed for neat graphite, while nickel ferrite shows stability over the entire temperature range up to 1000 °C as demonstrated in Figure S2 in the Supporting Information. DTG curves are presented in Figure 2e for the neat TPU polymer and G40NF5@TPU nanocomposite, while the DTG curves for graphite and nickel ferrite are presented in the Supporting Information (Figure S2). The DTG curves indicate that the maximum decomposition rates for the neat TPU matrix occur at approximately 345 and 406 °C. For the nanocomposite, the shoulder of the first peak at the low temperature coincides with the lowered degradation onset temperature. The first maximum of the nanocomposite's decomposition rate was observed at approximately 333 °C, which can be associated with the first decomposition step of the polymer matrix. The second decomposition step exhibits two poorly separated maxima at 393 and 412 °C. The corresponding mass loss is such that no other component than the second degradation step of the matrix can be associated with this step. The processing history and nanocomposite morphology may result in the separation of two processes that run indistinguishably in the neat polymer. The derivation of the TGA signal clearly revealed the last degradation step at 592 °C, which is associated with the degradation of graphite. The amount of char residue obtained after heating at 1000 °C was observed to be 40.3%. This is slightly less than 42.6% expected, according to the mass losses of the individual components. If this difference cannot be entirely attributed to experimental error, another source of the increased mass loss can be the reduction of nickel ferrite by carbon from the composite.[19] If all oxygen is removed, taking a corresponding amount of carbon in the form of CO away from the sample, the final mass loss of the sample would be 40.2%.

4.5. Mechanical Characteristics. Four samples of Pure TPU and G40NF5@TPU nanocomposites were prepared and tested for their mechanical properties. Figure 2f illustrates the stress−strain plot of the G40NF5@TPU nanocomposite. For comparison, the stress−strain curve for Pure TPU is illustrated in Figure S3a in the Supporting Information file. The **inset** in Figure S3a in the Supporting Information file demonstrates the digital pictures of the test samples of Pure TPU and the G40NF5@TPU nanocomposite for mechanical testing. Various parameters such as Young's modulus, elongation at break, and tensile strength for Pure TPU and G40NF5@TPU nanocomposite were calculated from the Stress−Strain curve and are plotted in Figure S3b−d in the Supporting Information file. The values of Young's modulus were 52.72 ± 3.43 and 127.62 ± 39.5 MPa for Pure TPU and G40NF5@TPU nanocomposite, respectively. A relatively high Young's modulus for the G40NF5@TPU nanocomposite indicated enhanced stiffness as compared to Pure TPU. Further, the evaluated value of tensile strength was 234.08 ± 13.04 and 36.16 ± 8.12 MPa for Pure TPU and G40NF5@TPU nanocomposite, respectively. The tensile strength of the G40NF5@TPU nanocomposite was significantly reduced compared to that of pure TPU. The contact of polymer chains was significant in pure TPU, but it was noticed to decrease with the addition of fillers. The high amount of filler loading can minimize interfiller distance and consequently lower the distance between polymer chains and nanoparticle fillers. Stronger filler−filler interactions outperform polymer−filler interactions, resulting in less load transfer between TPU and filler.[20] As a result, the tensile strength of the G40NF5@TPU nanocomposite is reduced. Furthermore, the values of elongation at break (%) were 916.18 ± 42.6% and 42.81 ± 6.671% for Pure TPU and G40NF5@TPU nanocomposite, respectively.

4.6. Surface-Wettability Properties. The application of EMI shielding materials in harsh environmental conditions highlights the importance of hydrophobicity in ensuring long-term durability and performance. The water contact angle (WCA) measurement serves as a key indicator of surface

https://doi.org/10.1021/acsanm.5c04619
ACS Appl. Nano Mater. 2026, 9, 353−369

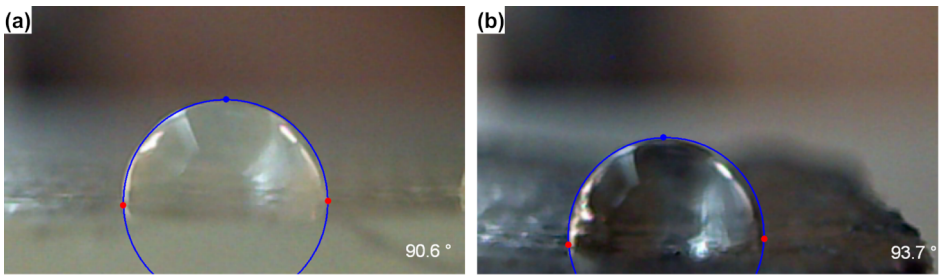

Figure 3. Water-contact angle measurements of (a) pure TPU and (b) the G40NF5@TPU nanocomposite.

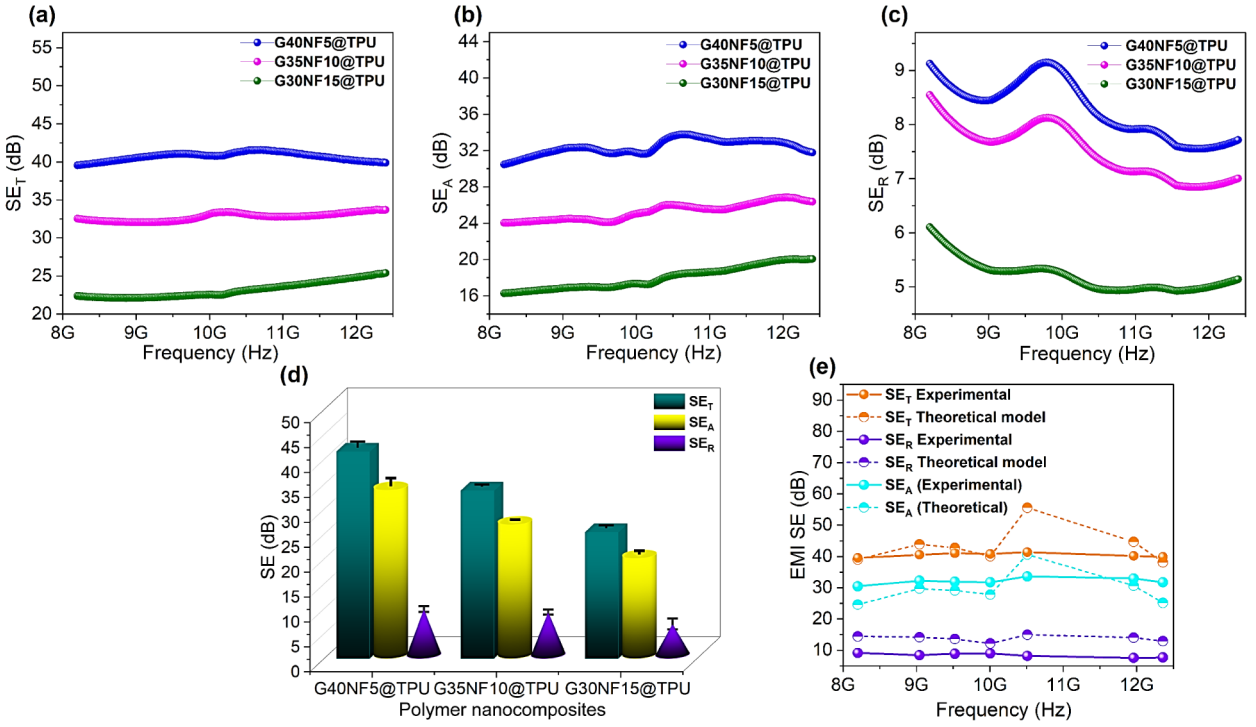

Figure 4. Frequency response of (a) SE_T, (b) SE_A, (c) SE_R, (d) comparison of EMI shielding parameters for GNF@TPU nanocomposites and (e) EMI shielding effectiveness of G40NF5@TPU nanocomposites obtained from the theoretical model and experimental measurements.

wettability, quantifying the interaction between a liquid droplet and the nanocomposite surface. A low WCA implies that the water droplet spreads easily over the surface, indicating hydrophilicity, while a high WCA suggests limited wettability and, thus, hydrophobic behavior. The Surface wettability is influenced by various factors, including chemical composition, filler−matrix interactions, synthesis methodology, and morphological features.[21] In this study, the WCA of pure TPU and the G40NF5@TPU nanocomposite was measured, as illustrated in Figure 3a−b. The WCA of pure TPU and the G40NF5@TPU nanocomposite was 90.6° and 93.7°, respectively. A contact angle greater than 90° typically signifies a hydrophobic surface. Although pure TPU exhibits marginal hydrophobicity, the increased WCA observed in the G40NF5@TPU nanocomposite reflects relatively an enhancement in surface hydrophobicity. The enhancement in water contact angle (WCA) can be attributed to increased surface roughness and the reduced surface energy of the developed nanocomposite, resulting from the incorporation of graphite and $NiFe_2O_4$ nanoparticles as fillers in pristine TPU.[22] This improved water-repellent behavior is advantageous for EMI shielding materials intended for use in harsh or moisture-rich environments.

4.7. EMI Shielding Application. A systematic study was performed to evaluate the EMI shielding behavior by measuring the EMI SE of the developed polymer nanocomposites in the X-band frequency region (8.2−12.4 GHz). Incident EM waves undergo three basic mechanisms on the surface of the EMI shielding material: reflection, absorption, and transmission. The total EMI shielding effectiveness, (SE_T) is generally described as a logarithmic term that quantifies the ratio of incident power (P_I) to transmitted power (P_T), and it can be mathematically represented as follows:

$$SE_T\ (dB) = 10\log\left(\frac{P_I}{P_T}\right)$$

The value of the SE_T is by adding the contributions from shielding due to absorption (SE_A), shielding due to reflection (SE_R) and shielding due to multiple reflections (SE_M) as demonstrated below:[23]

$$SE_T\ (dB) = SE_A + SE_R + SE_M$$

The contribution from shielding due to multiple reflections, SE_M is considered negligible if the value of SE_A exceeds 10 dB.

https://doi.org/10.1021/acsanm.5c04619
ACS Appl. Nano Mater. 2026, 9, 353−369

Table 1. A Comparison of EMI Shielding Materials Reported in the Literature with This Work

S.No.	Developed polymer nanocomposite	EMI SE	Thickness	Reference
1.	Polypyrrole-cobalt ferrite-graphene	37 dB	2.0 mm	28
2.	Graphite in polypropylene (PGP) composites	10.3 dB	-	29
3.	TPU/piperazine-modified ammonium polyphosphate (PA-APP)/$Ti_3C_2T_x$-salicylaldehyde-modified chitosan nanocomposites	21.3 dB	1.0 mm	30
4.	Graphene and $NiFe_2O_4$-PVDF hybrid polymer nanocomposites	22 dB	~0.2 mm	31
5.	Multi hierarchial TPU/cyclophosphazene functionalized $Ti_3C_2T_x$/Carbon fiber (CF) nanocomposite	30 dB	1.2 mm	32
6.	TPU/silicon wrapped ammonium polyphosphate polyphosphazene functionalized titanium carbide/carbon fiber fabric	27.4 dB	1.2 mm	33
7.	Hierarchical TPU/APP@LDH@Si/CP-PBM composites	43.6 dB	1.0 mm	18
8.	TPU-triazine-rich polyphosphazene functionalized MXene@copper phytate	29.7 dB	0.5 mm	34
9.	Chitosan-coated ammonium polyphosphate-MWCNTs-TPU composite	35.7 dB	1.00 mm	35
10.	Graphite-$NiFe_2O_4$ nanoparticles-TPU	41.6 dB	1.95 mm	**This work**

The calculations of SE_T, SE_A, and SE_R rely on the scattering parameters using the following expressions:[23]

$$SE_T = 10\log_{10}\left(\frac{1}{|S_{12}|^2}\right) = 10\log_{10}\left(\frac{1}{|S_{21}|^2}\right)$$

$$SE_R = 10\log_{10}\left(\frac{1}{|S_{11}|^2}\right)$$

$$SE_A = 10\log_{10}\left(\frac{1-|S_{11}|^2}{|S_{12}|^2}\right)$$

Where S_{11}, S_{22}, S_{12}, and S_{21} represent the forward reflection, backward reflection, forward transmission, and backward transmission scattering parameters, respectively.

Figure 4a–c demonstrates the variation of SE_T, SE_R, and SE_A as a response of frequency in the X-band region for G40NF5@TPU, G35NF10@TPU, and G30NF15@TPU polymer nanocomposites at a thickness of 1.95 mm. The maximum value of SE_T as depicted in Figure 4a was noticed to be 41.6 ± 1.14 dB, 33.8 ± 0.36 dB, and 25.0 ± 0.51 dB for G40NF5@TPU, G35NF10@TPU, and G30NF15@TPU polymer nanocomposites, respectively. Interestingly, the value of SE_T was observed to be highest for the G40NF5@TPU nanocomposite, having 40 wt % of graphite and 5 wt % of $NiFe_2O_4$ nanoparticles in the TPU matrix. Moreover, the value of SE_T was noted to decrease with a decrement in the wt % of graphite and an increase in the wt % of $NiFe_2O_4$ nanoparticles.[24] Additionally, the maximum value of SE_A as demonstrated in Figure 4b was measured to be 33.8 ± 1.59 dB, 26.8 ± 0.17 dB, and 20.10 ± 0.69 dB for G40NF5@TPU, G35NF10@TPU, and G30NF15@TPU respectively. The value of SE_R, as shown in Figure 4c for varied frequencies, reached maximum values of 9.1 ± 0.58 dB, 8.5 ± 0.50 dB, and 6.1 ± 1.08 dB for the G40NF5@TPU, G35NF10@TPU, and G30NF15@TPU polymer nanocomposites, respectively.

For a better understanding of the filler effects, the EMI SE of the TPU nanocomposites with pure graphite (G40@TPU) and $NiFe_2O_4$ nanoparticles (NF5@TPU) was also evaluated. Figure S4a–b in the Supporting Information file illustrates the frequency-dependent response of SE_T, SE_R, and SE_A for both polymer nanocomposites in the X-band frequency range. As can be seen, the maximum value of SE_T, SE_R, and SE_A for the G40@TPU nanocomposite was 18.68, 5.56, and 14.8 dB respectively, indicating a moderate EMI shielding performance. Further, the maximum value of SE_T, SE_R, and SE_A for the NF5@TPU nanocomposite was 0.63, 0.39, and 0.24 dB respectively, indicating poor SE. These results highlight that neither graphite nor $NiFe_2O_4$ nanoparticles alone provide substantial EMI shielding. The limited effectiveness of these fillers individually can be attributed to their distinct roles: graphite primarily contributes to the electrical conductivity and reflection of EM waves. At the same time, $NiFe_2O_4$ nanoparticles offer magnetic shielding but lack sufficient conductive properties to contribute effectively to EMI shielding on their own. However, when combined, the two fillers provide a synergistic effect: graphite enhances the electrical conductivity, improving reflection, while $NiFe_2O_4$ nanoparticles strengthen magnetic attenuation, improving overall shielding. This combination yields significantly higher EMI SE, underscoring the importance of filler synergy in enhancing material properties.

Additionally, Figure 4d presents a comparison of the individual contributions of SE_R, SE_A, and SE_T for all of the developed polymer nanocomposites. The analysis reveals that the primary contribution comes from SE_A rather than reflection for each of the prepared polymer nanocomposites. Since the value of $SE_T \geq 20$ dB is essential for commercial applications, all the polymer nanocomposites developed in this study demonstrated higher SE_T, positioning them as viable candidates for industrial use. The shielding efficiency percentage was assessed by using the following expression:

$$\text{Shielding Efficiency (\%)} = 100 - \left(\frac{1}{10^{SE/10}}\right) \times 100$$

The value of shielding efficiency (%) was found to be 99.99%, 99.95%, and 99.71% for G40NF5@TPU, G35NF10@TPU, and G30NF15@TPU polymer nanocomposites, respectively.

4.7.1. Theoretical Model. For analyzing the EMI shielding mechanism, Simon's formula was utilized to predict the theoretical EMI shielding performance for the G40NF5@TPU nanocomposite using the following expressions:[25]

$$SE_T\ (\text{dB}) = 10\log\frac{\sigma_T}{16f\varepsilon\mu_r} + 8.68t\frac{\sqrt{f\mu_r\sigma_T}}{2}$$

where σ_T corresponds to the total electrical conductivity of the material (in S/cm) and μ_r refers to the relative magnetic permeability of the material, ε refers to the electrical permittivity of the shielding material, and t corresponds to the thickness of the material (in m). Figure 4e illustrates the theoretical and experimental comparison of EMI shielding parameters such as SE_R, SE_A, and SE_T for the G40NF5@TPU

https://doi.org/10.1021/acsanm.5c04619
ACS Appl. Nano Mater. 2026, 9, 353–369

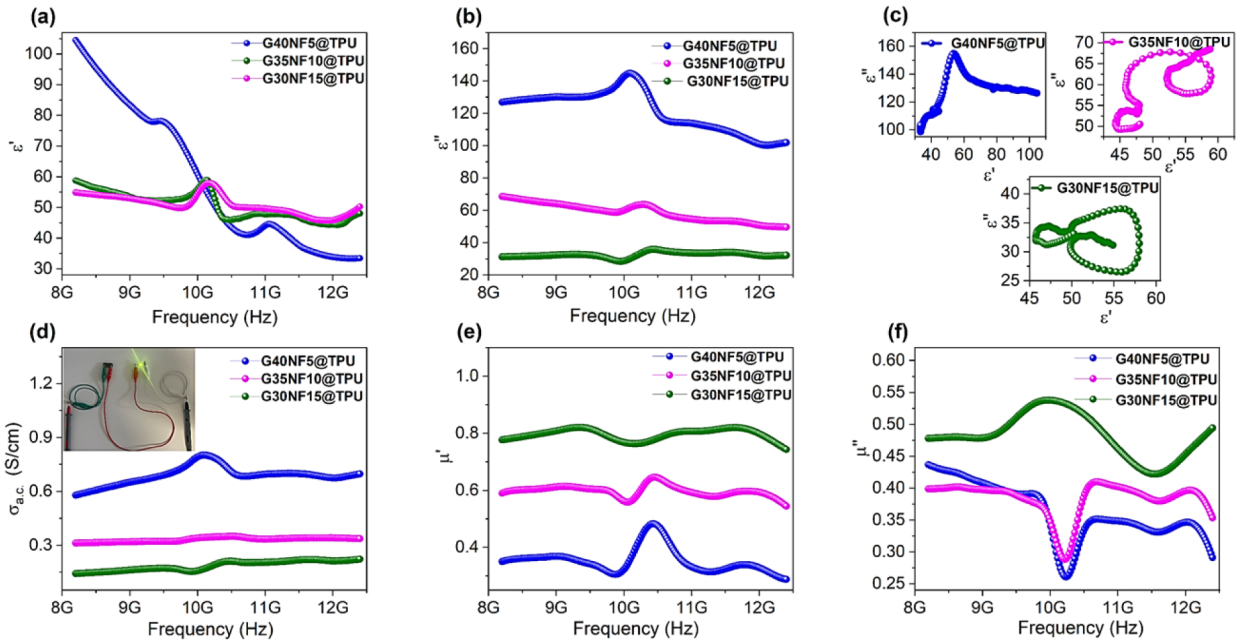

Figure 5. Frequency response of (a) the real part of permittivity ε', (b) the imaginary part of permittivity ε'', and (c) $\sigma_{a.c.}$ conductivity; inset: Visual demonstration of the electrical conductivity of the fabricated G40NF5@TPU nanocomposite, evidenced by LED illumination at a low driven voltage of 3 V in a simple circuit, (d) Cole−Cole plot, (e) the real part of permeability μ', and (f) the imaginary part of permeability μ'' of GNF@TPU nanocomposites.

nanocomposite with the variation of frequency in the X-band. As can be seen, the theoretically predicted values, as well as the trend with variation in frequency, were found to be closer to the experimentally obtained values of SE_R, SE_A, and SE_T. However, a sudden increase was noticed in the theoretical SE_T value at a frequency of 10.5 GHz, making the maximum value of SE_T higher than the experimental values obtained from the scattering parameters. Simon's formula assumes homogeneity in the tested sample with an assumption of uniform dispersion of the fillers. However, it is possible that the developed nanocomposite might not have uniform dispersion of the filler at some places in the matrix and, therefore, abrupt continuous conducting channels. Moreover, Simon's formalism does not consider dielectric losses, multiple reflections, and impedance mismatch that can influence the EMI SE performance of the nanocomposites.[25] Previously, Fang et al.[26] also noticed a slightly higher value of EMI SE for Ag Nanoparticle−Thiolated Chitosan Composite, evaluated using Simon's formula, compared with EMI SE measured experimentally. Another study by Yun et al.[27] also evaluated the value of SE_T for 2D $Ti_3C_2T_x$ MXene assembled film using Simon's formula and a significantly high value was noticed compared to the experimental values.[27] Notably, a higher value of SE_A compared to SE_R was observed both experimentally and theoretically, indicating absorption contributes more significantly than reflection to the overall SE_T value in the G40NF5@TPU nanocomposite.

Table 1 summarizes the performance of various polymer nanocomposites developed for electromagnetic interference (EMI) shielding reported in the literature.

Previous studies have demonstrated SE values typically ranging from 30 to 40 dB for systems utilizing hybrid fillers. In contrast, the nanocomposites developed in this study achieve a significant SE of 41.6 dB at a thickness of just 1.95 mm, outperforming many of the systems reported in the literature. This work also explores the influence of the optimal weight percentage of conductive and magnetic fillers, resulting in a substantial improvement over that of pure graphite or pure $NiFe_2O_4$-based TPU composites. The use of processing techniques and easily accessible graphite fillers further simplifies fabrication, leveraging to avoid complex processing steps while delivering excellent EMI shielding performance. Furthermore, as discussed in the following sections, the developed G40NF5@TPU nanocomposite exhibits outstanding Joule heating capabilities and efficient photothermal application, making the developed polymer nanocomposite suitable for multifunctional applications.

Thickness and density are two critical parameters to consider in designing an EMI shielding material. Taking this into account, the value of specific shielding effectiveness and absolute shielding effectiveness was evaluated using the following expressions:[36]

$$SSE = SE \times V/m$$

$$SSE_t = \frac{SSE}{t} = SE \times \frac{V}{m \times t}$$

where m refers to the mass, V represents the volume, and t depicts the thickness of the material. The value of SSE ranged from 20.8−32.5 $dBcm^3g^{-1}$ for the developed polymer nanocomposites. The observed values of SSE were higher than those reported for conventional metals such as copper (Cu: 10 $dBcm^3g^{-1}$), copper foil (7.8 $dBcm^3g^{-1}$), and stainless steel (11 $dBcm^3g^{-1}$), as previously reported in the literature.[37] Moreover, the value of absolute shielding effectiveness SSE_t ranged from 106−166.7 $dBcm^2g^{-1}$. Previously, Shen et al.[38] prepared Poly(ether imide)/Graphene@Fe_3O_4 composite foams and demonstrated an absolute shielding effectiveness SSE_t of 165 $dBcm^2g^{-1}$. Moreover, Chen et al. also reported an absolute shielding effectiveness SSE_t of 100.5 $dBcm^2g^{-1}$ for epoxy

https://doi.org/10.1021/acsanm.5c04619
ACS Appl. Nano Mater. 2026, 9, 353−369

nanocomposites reinforced with three-dimensional carbon nanotube sponge.[39]

4.8. Investigation of EM Parameters. *4.8.1. Complex Permittivity.* Complex permittivity and permeability play a significant role in effective microwave shielding. Therefore, considering this, complex permittivity and complex permeability are obtained using the inbuilt Nicholson−Ross−Weir approach. The real part of permittivity, ε', demonstrates the storage capacity of electric charges, whereas the imaginary part of permittivity, ε'', depicts the charge dissipation or losses. The real part of permittivity, ε', relates to the bound charges and polarizations. The imaginary part of permittivity ε'' is associated with the free charge carriers and attenuation of EM waves. Figure 5a represents the variation of ε' with frequency in the X-band region. The maximum value of ε' was 104.5 ± 1.45, 58.9 ± 0.02, and 57.9 ± 0.03 for the G40NF5@TPU, G35NF10@TPU, and G30NF15@TPU nanocomposites, respectively. With the highest ε' among all developed GNF@TPU polymer nanocomposites, the G40NF5@TPU nanocomposite stands out for its remarkable charge storage capacity. A decrease in the value of ε' with increasing frequency was observed for the G40NF5@TPU polymer nanocomposite. Upon applying an electrical field, the charge carriers present in the developed polymer nanocomposite can migrate and accumulate at the interfaces between the TPU polymer, $NiFe_2O_4$ nanoparticles, and graphite, leading to an increased ε'.[40] Similar behavior has been previously observed and reported by researchers in the literature.[41−43] In contrast, for the G35NF10@TPU and G30NF15@TPU nanocomposites, the reduced graphite content weakens the formation of continuous conducting pathways. Additionally, a higher concentration of $NiFe_2O_4$ nanoparticles can create agglomeration, which disrupts the conductive networks and further reduces the dielectric permittivity of the nanocomposites.

The plot of the ε'' versus frequency is presented in Figure 5b. As can be seen, the maximum value of ε'' was 144.6 ± 0.44, 68.6 ± 0.01, and 32.7 ± 0.01 for G40NF5@TPU, G35NF10@TPU, and G30NF15@TPU nanocomposites, respectively. The value of ε'' was maximum for the G40NF5@TPU nanocomposite among all the developed GNF@TPU polymer nanocomposites. The significant enhancement in ε'' for the G40NF5@TPU nanocomposite comprising 5 wt % of $NiFe_2O_4$ nanoparticles and 40 wt % of graphite demonstrates the role of multiple dipolar relaxation mechanisms. The dipolar relaxation process regulates the a.c. conductivity ($\sigma_{a.c.} = \omega\varepsilon_0\varepsilon''$) by generating dielectric losses.[24] In addition, a strong peak at ∼10.4 −10.5 GHz was noticed in the developed polymer nanocomposites. The asymmetric charge distribution at the tetrahedral and octahedral sites of $NiFe_2O_4$ nanoparticles contributes to the buildup of dipoles. Under an applied EM field, the orientation of dipoles leads to relaxation peaks.[44] Moreover, the value of ε'' was noticed to be higher than the value of ε' for the G40NF5@TPU polymer nanocomposite, which demonstrates the presence of a higher amount of charge carriers compared with bound charges.[45] The higher value of ε'' than ε' for the G40NF5@TPU nanocomposite is associated with dipole polarization resulting due to defects, and the existence of functional groups on the developed polymer nanocomposite due to two different phases in the TPU matrix.[46] The high values of ε' and ε'' confirmed the superior electric charge storage and attenuation capabilities of electrical energy in the G40NF5@TPU nanocomposite. For comparative analysis, the EM parameters of TPU nanocomposites containing individual fillers, graphite (G40@TPU), and the magnetic filler $NiFe_2O_4$ (NF5@TPU) were also evaluated, as shown in Figure S4c−d in the Supporting Information file. The maximum values of the real (ε') and imaginary (ε'') parts of the dielectric permittivity for the G40@TPU nanocomposite were approximately 84.6 and 30.0, respectively. In contrast, the NF5@TPU nanocomposite exhibited significantly lower ε' and ε'' values, with maxima of around 2.28 and 0.11, respectively. Further, it can be observed that the maximum value of ε' is relatively low for both G40@TPU and NF5@TPU nanocomposites compared with the combined G40NF5@TPU nanocomposite. This enhancement in ε' for the hybrid system can be attributed to the synergistic effect between the conductive graphite and magnetic $NiFe_2O_4$ nanoparticles, which promotes interfacial polarization and facilitates improved dipolar and space charge polarization within the TPU matrix. In the case of G40NF5@TPU, the highest loading of the conducting filler graphite (40 wt %) facilitates the formation of a well-connected conductive network within the polymer matrix. The high value of dielectric permittivity can be attributed to the generation of interfacial polarization due to the presence of defects and interfaces between multiple phases, such as nanoscopic $NiFe_2O_4$ nanoparticles and graphitic layers with different dielectric permittivity at external frequencies, resulting in higher dielectric losses.[47] The inclusion of magnetic $NiFe_2O_4$ nanoparticles in the developed TPU polymer nanocomposite, along with graphite, can promote a continuous conducting network, resulting in numerous heterogeneous surfaces and thereby enhancing polarization losses in the developed polymer nanocomposites.[48] The introduction of magnetic $NiFe_2O_4$ nanoparticles can influence the permittivity by tailoring the polarization and interfacial charge.[49]

4.8.2. Cole−Cole Plots. For a clear understanding of the role of the dipole relaxation phenomenon in the developed polymer nanocomposites, Debye theory has been widely adopted. On account of Debye's theory for dielectric loss properties, the values of ε' and ε'' can be expressed as follows:[10]

$$\varepsilon' = \varepsilon_\infty + \frac{\varepsilon_s - \varepsilon_\infty}{1 + (\omega\tau)^2}$$

$$\varepsilon'' = \frac{\varepsilon_s - \varepsilon_\infty}{1 + (\omega\tau)^2}\omega\tau + \frac{\sigma}{\omega\varepsilon_o}$$

where ε_∞ depicts the relative dielectric permittivity at an infinite frequency, ε_s represents the static dielectric permittivity, ω is the angular frequency, σ is the electrical conductivity, and τ refers for the polarization relaxation time, respectively. From the above equation, both ε' and ε'' are dependent on the value of $\omega\tau$ and thereby ε' and ε'' are independent of one another. However, if we neglect the role of σ to ε'' and eliminate $\omega\tau$, the equation between ε' and ε'' can be rewritten as follows:

$$\left(\varepsilon' - \frac{\varepsilon_s + \varepsilon_\infty}{2}\right)^2 + (\varepsilon'')^2 = \left(\frac{\varepsilon_s - \varepsilon_\infty}{2}\right)^2$$

According to the above-mentioned equation, ε'' vs ε' should be a semicircle, which is referred to as a Cole−Cole plot. Figure 5c depicts the Cole−Cole plots of GNF@TPU polymer nanocomposites at a frequency of 8.2−12.4 GHz. The presence of several semicircles in the Cole−Cole curves of the developed polymer nanocomposites indicates the involvement of polarization relaxation mechanisms.[50] The irregular

https://doi.org/10.1021/acsanm.5c04619
ACS Appl. Nano Mater. 2026, 9, 353−369

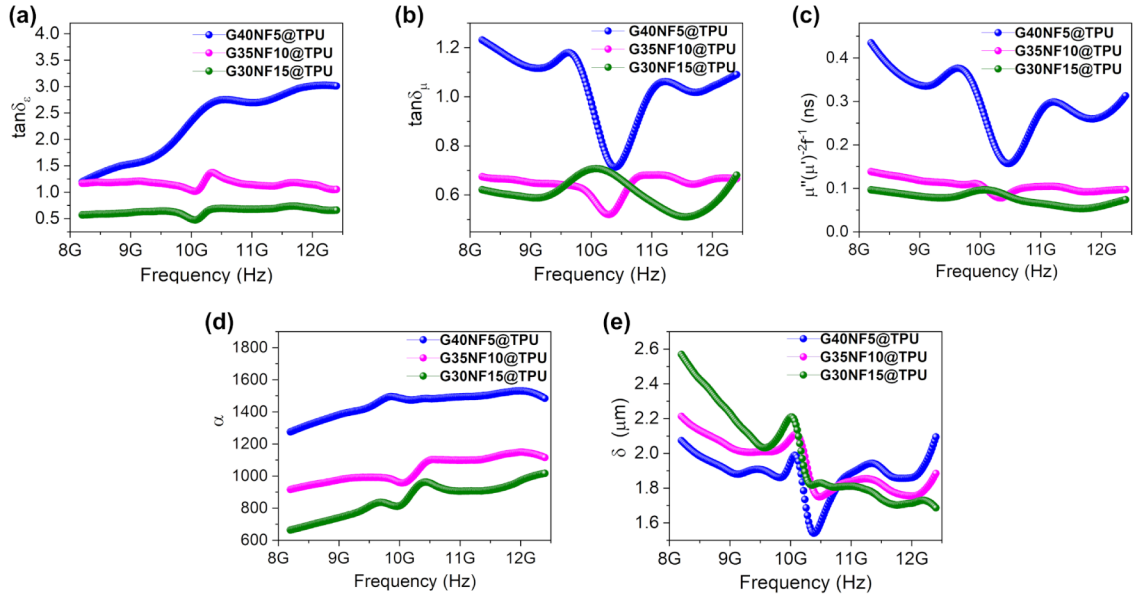

Figure 6. Frequency response curves of (a) dielectric loss tangent, tanδ_ε, (b) magnetic loss tangent, tanδ_μ of GNF@TPU polymer nanocomposites, (c) eddy current loss, C_0, (d) attenuation constant, α, and (e) skin depth, δ of GNF@TPU polymer nanocomposites.

shape of the Cole−Cole semicircles further highlights the significance of interfacial polarization in the GNF@TPU nanocomposites.[50] Moreover, a straight tail was also noticed, specifically for the G40NF5@TPU nanocomposite, confirming the contribution of conduction losses in the developed polymer nanocomposite system.

4.8.3. Electrical Conductivity. According to the free-electron theory, dielectric losses arise from conduction losses. Considering the contribution of conduction losses, the value of electrical conductivity was evaluated using the following expression:[10]

$$\varepsilon'' = \sigma_{a.c.}/2\pi\varepsilon_0 f$$

According to the equation, higher electrical conductivity can lead to an increase in the value of ε''. The electrical conductivity curve with a change in the frequency, shown in Figure 5d, indicates that the G40NF5@TPU nanocomposite exhibits the highest electrical conductivity. The maximum value of $\sigma_{a.c.}$ was 0.80 S cm^{-1}, 0.34 S cm^{-1}, and 0.22 S cm^{-1} for G40NF5@TPU, G35NF10@TPU, and G30NF15@TPU polymer nanocomposites, respectively. According to the general rule, the value of $\sigma_{a.c.}$ was noted to decrease with a decrease in the fraction loading of conducting filler graphite. The LED illumination test using a 3 V external power source, as shown in the inset of Figure 5d, further confirms the electrical conductivity of the G40NF5@TPU nanocomposite and its ability to form an efficient conductive pathway.

4.8.4. Complex Permeability. Figure 5e shows the real part of permeability (μ') as a frequency response. The maximum values of μ' were recorded as 0.51 ± 0.01, 0.64 ± 0.30, and 0.83 ± 0.32 for G40NF5@TPU, G35NF10@TPU, and G30NF15@TPU, respectively, indicating an increase in μ' with the higher weight percentage of magnetic filler in the polymer nanocomposite. Figure 5f illustrates the imaginary permeability (μ'') as a function of frequency, with maximum μ'' values ranging from 0.43 to 0.54 for the GNF@TPU polymer nanocomposites. As shown in Figure S4d in the Supporting Information file, the NF5@TPU nanocomposite exhibited maximum values of the real (μ') and imaginary (μ'') parts of magnetic permeability in the ranges of ∼1.19 and ∼0.01, respectively.

4.8.5. Dielectric and Magnetic Loss Tangents. The dielectric loss tangent, tanδ_ε = $\varepsilon''/\varepsilon'$ as a response to frequency, was evaluated and is demonstrated in Figure 6a. The highest values of tanδ_ε were found to be 3.0, 1.37, and 0.73 for the G40NF5@TPU, G35NF10@TPU, and G30NF15@TPU polymer nanocomposites, respectively. Notably, the tanδ_ε value for the G40NF5@TPU nanocomposite was significantly higher, reaching up to 3.0, compared to the other two nanocomposites. Dielectric losses play a primary role in energy attenuation within EMI shielding materials, and the high tanδ_ε value for G40NF5@TPU suggests an effective contribution of dielectric loss across the frequency range. The evaluation of the magnetic loss tangent tanδ_μ = μ''/μ' , generally characterizes the magnetic losses. The curve of tanδ_μ with variation of frequency is depicted in Figure 6b. As can be seen, the G40NF5@TPU nanocomposite exhibited the highest tanδ_μ with a maximum value of up to 1.23. Interestingly, two prominent peaks were noticed in the G40NF5@TPU polymer nanocomposite at frequencies ∼9.6 and ∼11.2 GHz, corresponding to the natural resonance and exchange resonance, respectively. Magnetic losses can originate from several factors, such as eddy current losses, domain-wall resonance, hysteresis loss, natural resonance, and exchange resonance.[11] However, domain-wall resonance and hysteresis loss contribute only at lower frequencies. Higher values of dielectric and magnetic loss tangents demonstrate the high capacity of the developed polymer nanocomposite to transform the EM wave energy into other forms of energy.[51] Therefore, an amalgam of dielectric and magnetic losses emerging from graphite and $NiFe_2O_4$ nanoparticles can help yield high EMI shielding properties.

4.8.6. Eddy Current Loss. The eddy current arises from the induced current generated by the magnetic component of the incident electric field. To understand the contribution of eddy current losses to the magnetic losses, the value of eddy current loss was evaluated using the following expression:[10]

https://doi.org/10.1021/acsanm.5c04619
ACS Appl. Nano Mater. 2026, 9, 353−369

Scheme 1. Illustrative Representation of EMI Shielding Mechanism of G40NF5@TPU Nanocomposite

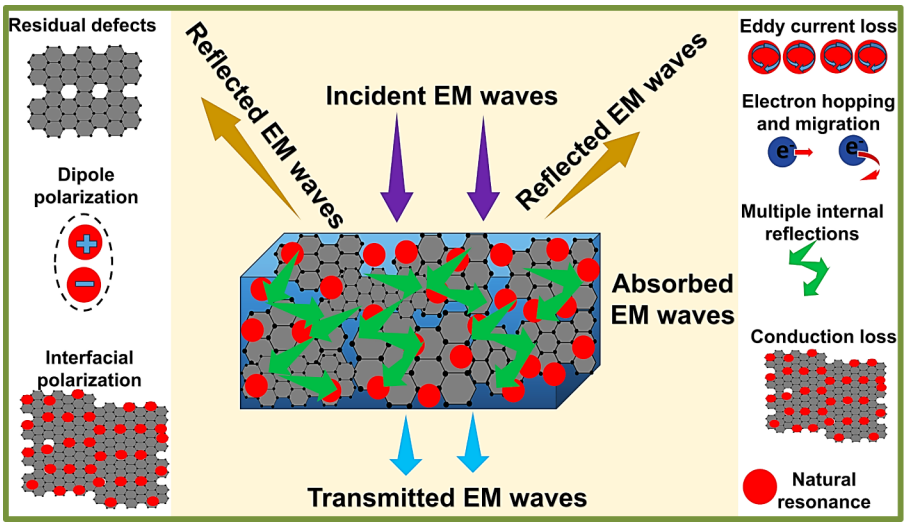

$$C_0 = \mu''(\mu')^{-2} f^{-1}$$

In the above expression, if the value of C_0 remains independent with variation of frequency, then there is a contribution of eddy current losses.[52] Figure 6c illustrates the response curve of eddy current loss with a change in frequency. As can be seen, for the G40NF5@TPU polymer nanocomposite, the value of C_0 is found to be nearly constant from 9.5 to 9.9 GHz, 10.3 to 10.7 GHz, 11.1 to 11.6 GHz, and 12.3 to 12.4 GHz. Two prominent magnetic resonance peaks were observed at frequencies around 9.6 and 11.2 GHz, corresponding to natural resonance and exchange resonance, respectively.[52,53] Natural resonance can arise from the distribution of $NiFe_2O_4$ nanoparticles in the TPU matrix.[54] The nanoscale $NiFe_2O_4$ nanoparticles, along with the introduction of nonmagnetic graphite filler, might have contributed to the natural resonance. Moreover, exchange resonance is expected due to the magnetic coupling effect caused by the $NiFe_2O_4$ nanoparticles in the TPU matrix.[54] Therefore, it can be concluded that the primary originator of magnetic loss is from the eddy current effect, natural resonance, and exchange resonance.

4.8.7. Attenuation Constant. In addition to the dielectric and magnetic losses, the attenuation constant also plays a significant part in the efficient EMI shielding properties of the material. The attenuation constant, which quantifies the EMI shielding material's ability to attenuate incoming EM waves, can be calculated using the following expression[55]

$$\alpha = \frac{\sqrt{2}\,\pi f}{c} \sqrt{(\mu''\varepsilon'' - \mu'\varepsilon') + \sqrt{(\mu''\varepsilon'' - \mu'\varepsilon')^2 + (\varepsilon'\mu'' + \varepsilon''\mu')^2}}$$

where c corresponds to the speed of light in vacuum.

The attenuation constant was assessed and is represented in Figure 6d as a function of the frequency. It can be noticed that the value of α is immensely high for the G40NF5@TPU nanocomposite, which is composed of 5 wt % $NiFe_2O_4$ nanoparticles and 40 wt % graphite. This high value can be directly correlated with the high value of SE_T in the developed GNF@TPU polymer nanocomposites. The high value of SE_T is expected to originate from high dielectric losses, magnetic losses, conduction losses, and a high value of the attenuation constant.

4.8.8. Skin Depth. As the incident EM wave travels further into the surface of the material, it diminishes dramatically. Skin depth determines the distance traveled by the EM wave before it attenuates and reduces to 1/e (37%) of the incident wave. In general, materials with high conductivity and low skin depth are considered suitable for EMI shielding at higher frequencies.[56] The value of skin depth can be evaluated using the mathematical expression as follows:[10]

$$\delta = \frac{1}{\sqrt{\pi \mu \sigma f}}$$

The value of δ was evaluated using the expression mentioned above and is plotted with a variation of frequency in Figure 6e. The highest values of δ were found to be 2.09 μm, 2.21 μm, and 2.56 μm for the G40NF5@TPU, G35NF10@TPU, and G30NF15@TPU nanocomposites, respectively. The value of δ was lowest for the G40NF5@TPU nanocomposite. Moreover, with increasing frequency, skin depth was observed to be reduced, thereby demonstrating higher attenuation of EM waves in the G40NF5@TPU nanocomposite. Low skin depth is a crucial factor in defining the EMI shielding performance of materials.

4.8.9. EMI Shielding Mechanism. The EMI shielding mechanism of the G40NF5@TPU nanocomposite, which incorporates graphite as an electrically conductive filler and $NiFe_2O_4$ nanoparticles as a magnetic filler, is illustrated in Scheme 1. When EM waves strike the surface of the G40NF5@TPU nanocomposite, an impedance mismatch occurs. Consequently, some of the EM waves are instantly reflected, while the remaining waves enter the composite. The interfacial impedance mismatch causes the EM waves in the G40NF5@TPU nanocomposite to be absorbed due to dielectric, conduction, and magnetic losses.[57]

The absorbed EM waves undergo multiple internal reflections, thereby enhancing the EM wave dissipation in the G40NF5@TPU nanocomposite. The EMI shielding mechanism of the G40NF5@TPU nanocomposite is influenced by various factors, including dielectric losses, magnetic losses, conduction losses, and multiple internal reflections, which collectively reduce the EM energy. According to Debye's

https://doi.org/10.1021/acsanm.5c04619
ACS Appl. Nano Mater. 2026, 9, 353−369

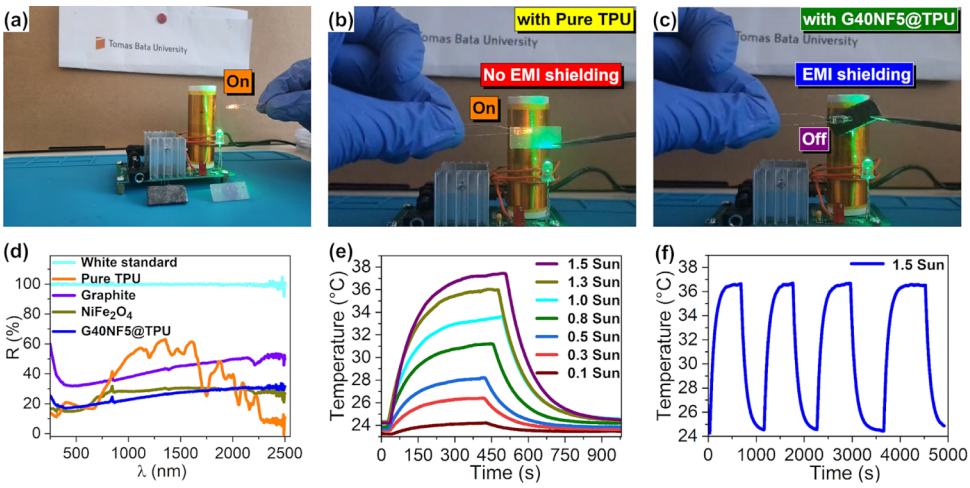

Figure 7. Experimental visualization of electromagnetic interference (EMI) shielding behavior using a Tesla coil setup: (a) Illumination of the bulb in proximity to the Tesla coil due to emitted electromagnetic radiation, (b) continued bulb illumination when pure TPU is introduced as a barrier, (c) complete suppression of bulb illumination upon the introduction of the G40NF5@TPU nanocomposite as a barrier, demonstrating its superior EMI shielding performance, (d) UV−vis spectra of the G40NF5@TPU nanocomposite along with its all the components, (e) Photothermal response of G40NF5@TPU, (f) stability test of the G40NF5@TPU nanocomposite.

theory, the dielectric loss properties, represented by ε'' consist of polarization loss and conduction loss. In the G40NF5@TPU nanocomposite, polarization primarily occurs through interfacial and dipole polarization. Interfacial polarization arises from the numerous interfaces between graphite and $NiFe_2O_4$ nanoparticles, contributing to the attenuation of the EM waves.[8] Dipole polarization is a result of functional groups, defects, and the uneven distribution of charges on the graphite and $NiFe_2O_4$ surface. Graphite as well as $NiFe_2O_4$ nanoparticles forms a conductive network that facilitates electron hopping and migration,[58] as shown in Scheme 1. The unique structure of $NiFe_2O_4$ nanoparticles not only improves dielectric losses but also enhances magnetic losses, resulting in magnetic-dielectric synergy. $NiFe_2O_4$ nanoparticles can absorb EM waves and transfer them into heat losses originating due to vibration in the crystal after EM wave absorption.[24] Magnetic losses originate from various factors, such as eddy current loss, natural resonance, and exchange resonance. By optimizing the weight percentages of graphite and $NiFe_2O_4$ nanoparticles, a balance between dielectric and magnetic losses is achieved, leading to superior EMI shielding performance.[59]

4.8.10. Practical Demonstration of EMI Shielding. A wireless transmission system based on a Tesla coil was used to visualize the EMI shielding performance of the G40NF5@TPU nanocomposite, as demonstrated in Figure 7. When the circuit is activated, the varying current in the primary coil induces a high voltage in the secondary coil, leading to the formation of an electromagnetic field. As a result, the bulb glows even with a minimal current generation due to electromagnetic induction. As can be seen in Figure 7a, when the switch is "on", the bulb glows bright. In Figure 7b, when Pure TPU is brought close to the Tesla coil circuit, the bulb still glows. However, when the G40NF5@TPU nanocomposite was brought in proximity to the Tesla coil circuit (Figure 7c), the bulb turned "off", thereby confirming the ability of the developed G40NF5@TPU nanocomposite to block the high-frequency EM waves emitted by the Tesla coil. A video demonstration (Video S1 in the Supporting Information file) clearly shows the bulb's response in the presence and absence of the Pure TPU and G40NF5@TPU nanocomposite as shielding material. This demonstration serves as concrete proof of the EMI shielding capabilities of the G40NF5@TPU nanocomposite, positioning it as a promising candidate for practical applications.

4.9. Photothermal Properties. The developed G40NF5@TPU nanocomposite can absorb solar light significantly, as can be deduced from the reflectance spectrum in Figure 7d. The reflectance of the material is only 25% on average over the range from 250 to 2500 nm, which means that the material reflects with respect to the solar irradiance only 20.8% of incident solar light energy, while the complementary 79.1% is absorbed. These values are calculated according to ISO 22969:2019 (E) using the AM1.0 reference global solar radiation at sea level. As the sample is opaque (zero transmittance) and there is no photoluminescence or light energy transformation other than to generate heat, the material has potential for photothermal applications. The graph in Figure 7d also presents spectra of the components used for the preparation of the nanocomposite. The spectrum of nickel ferrite powder is similar to the spectrum of graphite, both resembling gray diffusion reflectance standards in appearance. It can also be observed that the graphite spectral feature dominates the spectrum of the resulting material, while only negligible contributions to the polymer matrix are manifested. The contribution of nickel ferrite is not pronounced due to its low content as well as its similarity to the graphite spectral response. This is in accordance with a slight graphitic shine appearance of the prepared nanocomposite. Nevertheless, on average, the reflectance of the nanocomposite's surface was nearly two times suppressed in comparison with the neat graphite due to the compounding procedure with the other components.

The photothermal performance of the developed G40NF5@TPU nanocomposite was systematically evaluated under AM1.5G solar-simulated light irradiation, where 1 Sun corresponds to an intensity of 87.5 ± 4.3 mW cm^{-2} integrated over the used wavelength range from 350 to 1450 nm. The digital photograph in Figure S5a of the Supporting Information file demonstrates the G40NF5@TPU nanocomposite under simulated solar light irradiation using a setup similar to that

https://doi.org/10.1021/acsanm.5c04619
ACS Appl. Nano Mater. 2026, 9, 353−369

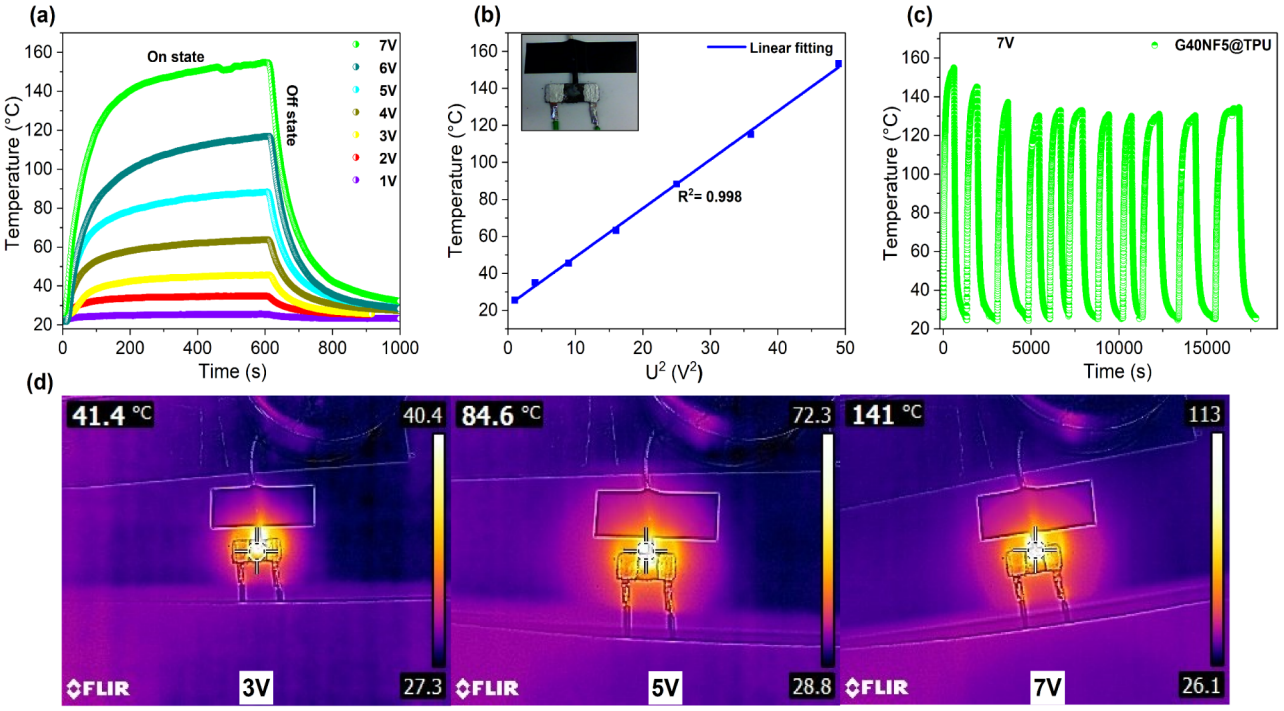

Figure 8. Joule heating performance of the G40NF5@TPU nanocomposite. (a) Time-dependent temperature response during alternating "on" and "off" states of the input voltage 1 V−7 V, (b) Long-term cyclic stability in "on" and "off" states of the input voltage (7 V), (c) Steady-state temperature as a function of the square of the applied voltage (Inset: Digital image of the tested G40NF5@TPU nanocomposite), and (d) Infrared (IR) images illustrating temperature variation with increasing voltage.

typically referred to in the literature.[60] The sample is irradiated from the top while resting on a thermal insulation support, and the surrounding laboratory acts as a thermal sink. Evaluating the measured reflectance spectrum with respect to the AM1.5G spectral energy distribution (according to ASTM G-173-03) in the spectral range provided by the used solar simulator indicates the absorption of 80.0% of incident light energy, corresponding to an input power of 70.0 ± 3.4 mW cm^{-2} to the sample. The corresponding calculation is provided in the Supporting Information. As can be seen in Figure 7e, under simulated solar illumination, the G40NF5@TPU nanocomposite sample exhibited an increase in temperature nearly up to the saturation temperature, when the light power input equilibrated with the heat transfer to the surroundings, working as the thermal sink. When the light is off, a characteristic exponential decrease in temperature is also observed. A gradual increase in the saturation temperature with increasing light intensity is clearly evident. Specifically, the saturation temperatures recorded were approximately 24 °C, 26 °C, 28 °C, 31 °C, 33 °C, 35 °C, and 37 °C under irradiation levels of 0.1, 0.3, 0.5, 0.8, 1.0, 1.3, and 1.5 Sun, respectively. While the absolute values of the saturation temperature depend on the heat transfer coefficient to the surroundings of the sample, the relative trend confirms the material's photosensitivity and efficient light-to-heat conversion capability. Previously Guo et al.[61] developed Aramid Nanofiber/Polypyrrole composite films and reported a photothermal response with a saturation temperature reaching up to 62 °C under irradiation of 150 mW cm^{-2} which is greater than the power intensity of 1.5 Sun (129.1 mW cm^{-2}) utilized in this work. Further, another researcher Zhang et al.[60] demonstrated photothermal performance for CNTs@MXene heterostructure-decorated cellulose films with a saturation temperature of up to 55 °C under irradiation levels of 1.5 Sun. The photothermal heating mechanism can be attributed to the absorption of photons, leading to electron excitation to higher energy states. These excited electrons subsequently interact with phonons, resulting in nonradiative relaxation and heat generation within the material matrix.[62] The infrared (IR) thermal image presented in Figure S5b in the Supporting Information file visually confirms the temperature increase on the nanocomposite surface under simulated sunlight, further validating the correspondence between the surface temperature and the sample's temperature measured from its bottom side. No overheating of the irradiated surface was observed, indicating good thermal conductivity, ensuring sufficient homogeneity of the generated heat distribution throughout the sample volume under a given irradiation power.

To evaluate the thermal stability and repeatability, cyclic photothermal tests of the developed G40NF5@TPU nanocomposite for photothermal response were conducted under 1.5 Sun irradiation, as demonstrated in Figure 7f. The G40NF5@TPU nanocomposite consistently maintained its saturation (surface) temperature across multiple cycles, indicating the thermal stability and reproducibility of its photothermal behavior.

4.10. Joule Heating Performance. In addition to EMI shielding, electrical heating is a crucial feature that enables the developed polymer nanocomposite to provide multiple functions efficiently in cold environments.[16] According to the Joule's effect, when a DC current flows through a conductor, heat is generated at a rate P as per the given expression:[63]

$$P = \frac{U^2}{R}$$

https://doi.org/10.1021/acsanm.5c04619
ACS Appl. Nano Mater. 2026, 9, 353−369

Where P signifies the Joule heating rate (in Watts), U is the input voltage, and R represents the resistance, which is assumed constant for the sake of simplicity. The developed G40NF5@TPU nanocomposite exhibits significant electrical conductivity and could be a suitable candidate for testing its Joule heating performance.[64] Materials with Joule heating capabilities can be tuned to reach specific target temperatures, as required. Considering this, the G40NF5@TPU nanocomposite was tested for its Joule heating performance by measuring the heat generated at varying input voltages from 1 to 7 V.

Figure 8a shows the temperature response of the G40NF5@TPU nanocomposite over time for input voltages ranging from 1 to 7 V. Upon applying a driving voltage, the temperature of the G40NF5@TPU nanocomposite increases due to Joule heating, which arises from the inelastic collisions between accelerated electrons and phonons as expected for a material with purely resistive behavior.[65] The temperature was monitored for up to 600 s, demonstrating long-term stability. The surface temperature increased sharply within the first 100−200 s after the voltage was applied, then the increase slowed down, following a common simple exponential growth trend. The maximum temperature achieved at 600 s can be considered a good approach to a thermal steady state when the Joule heating rate is balanced by the combined radiative and convective heat losses to the surroundings working as the heat sink, similar to the Photothermal experiment.[66] While the temperature of the G40NF5@TPU nanocomposite did not rise significantly at an input voltage of 1 V, a further increase in input voltage resulted in a notable rise in steady-state temperature, reaching approximately ∼154.4 °C at 7 V. To summarize, it was observed that the surface temperature of the G40NF5@TPU nanocomposite reached ∼25.6 °C, ∼35.1 °C, ∼45.6 °C, ∼63.3 °C, ∼88.3 °C, ∼115.2 °C, and ∼154.4 °C at constant input voltages of 1, 2, 3, 4, 5, 6, and 7 V, respectively. After the electrical power was switched off at 600 s, the sample cooled naturally down to the laboratory temperature.

Previously, Wei et al.[65] demonstrated the Joule-heating capabilities of an Aramid nanofiber incorporated with carbon nanotubes and cobalt ferrite nanoparticles aerogel film, where its surface temperature reached up to 110 °C with a driven voltage of 9 V. Wang et al.[67] demonstrated the Joule heating effect for a Polystyrene−polyisoprene−polystyrene coated Fe3C−C/MXene composite film with a surface temperature of 63.5 °C with an input voltage of 6 V. It should be noted that the final maximum temperature value corresponds to the balance between the electrical power dissipation through Joule heating and the heat loss rate to the surroundings, which was the laboratory environment in all reported examples. No forced cooling or special arrangement different from ours was noted, indicating the approximate comparability of the results.

In our case, the temperature stabilized at approximately 154 °C with a voltage of 7 V, despite continuous heating of the nanocomposite only for approximately 600 s. It should be noted that the input voltage is safe for humans, as it was operated at less than 36.0 V, and therefore can also be utilized in wearable heating devices.[68] The steady-state temperature shown in Figure 8b displayed a linear correlation with the square of the voltage (V^2), in alignment with Joule's law, suggesting a well-controlled Joule heating performance as well as the dissipative heat losses to the surroundings in the laboratory environment. To further evaluate the robustness of the Joule heating performance, cyclic heating and cooling were tested by repeatedly applying and releasing the input voltage. Figure 8c displays the cyclic stability test of the G40NF5@TPU nanocomposite performed for 11 cycles at the "on" and "off" states at the input voltage of 7 V. As can be seen, initially, the surface temperature of the G40NF5@TPU nanocomposite was in the range of ∼155 °C to ∼145 °C. After 1−2 cycles, the thermal response of the G40NF5@TPU nanocomposite was stabilized in the range of ∼135 °C with negligible variation. This confirmed the excellent cyclic stability of the developed G40NF5@TPU nanocomposite, making it suitable for industrial applications. To visualize the changes in surface temperature, a series of thermal infrared images for 3, 5, and 7 V were captured, clearly illustrating the temperature variations across the G40NF5@TPU nanocomposite, as demonstrated in Figure 8d. In conclusion, the G40NF5@TPU nanocomposite, with its excellent Joule heating response and stable operation, shows great potential for industrial applications, including electro-thermal garments and thermotherapy wearable devices, as well as controllable heating elements.[69]

5. CONCLUSION

In summary, various sets of TPU-based nanocomposites were incorporated with varying loadings of electrically conducting graphite and magnetic $NiFe_2O_4$ nanoparticle filler using a melt-mixing approach. The developed G40NF5@TPU nanocomposite, comprising 40 wt % graphite and 5 wt % $NiFe_2O_4$ nanoparticles, demonstrated superior EMI shielding characteristics with a total EMI shielding effectiveness of 41.6 dB in the 8.2−12.4 GHz (X-bandwidth) range at a thickness of only 1.95 mm. All the developed GNF@TPU-based nanocomposites can be utilized for commercial applications since all of them demonstrate shielding effectiveness ≥20 dB in the X-band frequency range. The shielding efficiency values (%) were found to be 99.99%, 99.95%, and 99.71% for G40NF5@TPU, G35NF10@TPU, and G30NF15@TPU polymer nanocomposites, respectively. The value of SSE ranged from 20.8 to 32.5 $dBcm^3g^{-1}$ for the developed GNF@TPU polymer nanocomposites. Additionally, the absolute shielding effectiveness SSE_t of the developed GNF@TPU polymer nanocomposites ranged from 106−166.7 $dBcm^2g^{-1}$. The EMI shielding performance of the G40NF5@TPU nanocomposite was contributed by several factors, including high dielectric and conduction losses, moderate magnetic loss, and eddy current loss, resulting in a high attenuation constant. The developed G40NF5@TPU nanocomposites also demonstrated stable and efficient photothermal response with surface temperature reaching up to ∼37 °C within 400 s, under solar-simulated irradiation. In addition, the G40NF5@TPU nanocomposite, benefiting from its high electrical conductivity, showcased stable and controlled Joule heating performance with a rapid thermal response reaching surface temperature up to ∼154 °C at a low driven input voltage of 7 V under given laboratory dissipative heat loss conditions. In addition, the improved hydrophobic property of the developed G40NF5@TPU nanocomposite makes it suitable for use in moisture-rich environments. These multifunctional properties, including superior EMI shielding, excellent Joule heating, and stable, efficient photothermal conversion, and hydrophobicity, position the G40NF5@TPU nanocomposite as a promising material for applications in wearable electronic devices, personal heating systems, defense technologies, aerospace applications, and other industries that require effective EMI shielding and thermal management.

https://doi.org/10.1021/acsanm.5c04619
ACS Appl. Nano Mater. 2026, 9, 353−369

■ ASSOCIATED CONTENT

Supporting Information

The Supporting Information is available free of charge at https://pubs.acs.org/doi/10.1021/acsanm.5c04619.

Preparation of $NiFe_2O_4$ nanoparticles and their developed GNF@TPU nanocomposites, Fabrication of GNF@TPU nanocomposites with variation of wt % graphite and $NiFe_2O_4$ nanoparticles, Composition of G40NF5@TPU nanocomposites using EDX spectra, Evaluation of magnetic parameters for developed GNF@TPU polymer nanocomposites, TGA and DTG of individual fillers, Mechanical characteristics, EMI shielding and EM parameters study for TPU nanocomposites based on individual fillers, Digital and IR image of the G40NF5@TPU nanocomposite under solar simulator, Solar power reflectivity and absorption evaluation (PDF)

Demonstration of EMI shielding capability of developed nanocomposite using Tesla coil (MP4)

■ AUTHOR INFORMATION

Corresponding Author

Raghvendra Singh Yadav − *Centre of Polymer Systems, University Institute, Tomas Bata University in Zlín, Zlín 760 01, Czech Republic;* orcid.org/0000-0003-1773-3596; Phone: +420 576 031 725; Email: yadav@utb.cz

Authors

Anju − *Centre of Polymer Systems, University Institute, Tomas Bata University in Zlín, Zlín 760 01, Czech Republic;* orcid.org/0000-0001-9321-7089

Milan Masař − *Centre of Polymer Systems, University Institute, Tomas Bata University in Zlín, Zlín 760 01, Czech Republic*

Michal Machovský − *Centre of Polymer Systems, University Institute, Tomas Bata University in Zlín, Zlín 760 01, Czech Republic;* orcid.org/0000-0003-4825-968X

Michal Urbánek − *Centre of Polymer Systems, University Institute, Tomas Bata University in Zlín, Zlín 760 01, Czech Republic*

Pavol Šuly − *Centre of Polymer Systems, University Institute, Tomas Bata University in Zlín, Zlín 760 01, Czech Republic;* orcid.org/0000-0002-7500-7800

Jiří Matyáš − *Centre of Polymer Systems, University Institute, Tomas Bata University in Zlín, Zlín 760 01, Czech Republic*

Jarmila Vilčáková − *Centre of Polymer Systems, University Institute, Tomas Bata University in Zlín, Zlín 760 01, Czech Republic;* orcid.org/0000-0002-1216-2862

Ivo Kuřitka − *Centre of Polymer Systems, University Institute, Tomas Bata University in Zlín, Zlín 760 01, Czech Republic;* orcid.org/0000-0002-1016-5170

Complete contact information is available at: https://pubs.acs.org/10.1021/acsanm.5c04619

Author Contributions

The manuscript was written through contributions of all authors. All authors have given approval to the final version of the manuscript.

Notes

The authors declare no competing financial interest.

■ ACKNOWLEDGMENTS

This work was supported by the financial grant provided by the Ministry of Education, Youth and Sports of the Czech Republic—DKRVO (RP/CPS/2024-28/007).

■ REFERENCES

(1) Gong, X.; Hu, T.; Zhang, Y.; Zeng, Y.; Zhang, Y.; Jiang, Z.; Tan, Y.; Zou, Y.; Wang, J.; Dai, J.; Chu, Z. Trunk-Inspired SWCNT-Based Wrinkled Films for Highly-Stretchable Electromagnetic Interference Shielding and Wearable Thermotherapy. *Nanomicro Lett.* **2024**, *16* (1), 243.

(2) Liu, S.; Qin, S.; He, M.; Zhang, D.; Shi, Y.; Huang, F.; Song, P. Construction and Application of Flexible Electromagnetic Interference Shielding Films with Multifunctionality. *Compos. Commun.* **2024**, *50*, 102011.

(3) Wang, L.; Xu, D.; Zhou, J. Multilayer Composite Films with Enhanced Electromagnetic Interference Shielding and Thermal Management Properties Based on Bamboo Cellulose Nanofibers. *Carbohydr. Polym.* **2025**, *354*, 123309.

(4) Feng, Q. -H.; Liu, J.; Shen, Y. -B.; Cao, C. -F.; Hu, W. -Y.; Liu, T. -T.; Fu, Y. -G.; Qi-Shi; Wan, J. -J.; Lv, P. -Y.; et al. Mechanically Flexible, Water-Resistant, and Flame-Retardant Sodium Alginate/Montmorillonite-Based Nanocomposite for Fire Alarm and Protection. *Compos. Part A Appl. Sci. Manuf.* **2025**, *190*, 108662.

(5) Chen, Z. Y.; Wu, Y. Y.; Liu, S. C.; Li, Y.; Guan, Z. Q.; Cao, C. F.; Zhang, G. D.; Tuten, B. T.; Gao, J. F.; Shi, Y. Q.; Song, P.; Tang, L. C. Pottery-Inspired Flexible Fire-Shielding Ceramifiable Silicone Foams for Exceptional Long-Term Thermal Protection. *Adv. Funct. Mater.* **2025**, *35* (3), 2413362.

(6) Chen, K.; Liu, M.; Shi, Y.; Wang, H.; Fu, L.; Feng, Y.; Song, P. Multi-Hierarchical Flexible Composites towards Superior Fire Safety and Electromagnetic Interference Shielding. *Nano Res.* **2022**, *15* (10), 9531−9543.

(7) Jeong, H. O.; Hossain, M. M.; Lim, H.; Kim, Y. K.; Kim, J.; Jeong, H. D.; Cho, H.; Goh, M.; Kim, M. J.; You, N. H.; Jeong, K. U.; Hahn, J. R.; Jang, S. G. Nanoscale Brick and Mortar Strategy for Mechanically Strong Multifunctional Composites with Extremely High Filler-Loading. *Carbon* **2024**, *226*, 119198.

(8) Ma, M.; Liang, X.; Tao, W.; Peng, Q.; Shao, W.; Chen, S.; Shi, Y.; He, H.; Zhu, Y.; Wang, X. Waterborne Polyurethane Aerogel with Asymmetric Gradient Structure Formed by Density-Induced Self-Stratification for Absorption-Dominated Electromagnetic Interference Shielding. *Compos. Struct.* **2024**, *342*, 118259.

(9) Liu, M.; Wang, Z.; Song, Z.; Wang, F.; Zhao, G.; Zhu, H.; Jia, Z.; Guo, Z.; Kang, F.; Yang, C. A Popcorn-Inspired Strategy for Compounding Graphene@$NiFe_2O_4$ Flexible Films for Strong Electromagnetic Interference Shielding and Absorption. *Nat. Commun.* **2024**, *15* (1), 5486.

(10) Anju; Milan, M.; Machovsky, M.; Urbánek, M.; Šuly, P.; Hanulíková, B.; Vilčáková, J.; Kuřitka, I.; Yadav, R. S. Optimization of $CoFe_2O_4$ Nanoparticles and Graphite Fillers to Endow Thermoplastic Polyurethane Nanocomposites with Superior Electromagnetic Interference Shielding Performance. *Nanoscale Adv.* **2024**, *6* (8), 2149−2165.

(11) Yadav, R. S.; Kuřitka, I.; Vilcakova, J.; Skoda, D.; Urbánek, P.; Machovsky, M.; Masař, M.; Kalina, L.; Havlica, J. Lightweight $NiFe_2O_4$-Reduced Graphene Oxide-Elastomer Nanocomposite Flexible Sheet for Electromagnetic Interference Shielding Application. *Compos. B Eng.* **2019**, *166*, 95−111.

(12) Anand, S.; Pauline, S. Electromagnetic Interference Shielding Properties of $BaCo_2Fe_{16}O_{27}$ Nanoplatelets and RGO Reinforced PVDF Polymer Composite Flexible Films. *Adv. Mater. Interfaces* **2021**, *8* (3), 2001810.

(13) Hariharasuthan, R.; Chitradevi, S.; Radha, K. S.; Chithambaram, V. Characterization of $NiFe_2O_4$ (Nickel Ferrite) Nanoparticles with Very Low Magnetic Saturation Synthesized via Co-Precipitation Method. *Appl. Phys. A* **2022**, *128*, 1045.

(14) Prabhakaran, T.; Hemalatha, J. Chemical Control on the Size and Properties of Nano $NiFe_2O_4$ Synthesized by Sol−Gel Autocombustion Method. *Ceram. Int.* **2014**, *40* (2), 3315−3324.
(15) Pulikkalparambil, H.; Saravana Kumar, M.; Babu, A.; Ayyappan, V.; Tengsuthiwat, J.; Rangappa, S. M.; Siengchin, S. Effect of Graphite Fillers on Woven Bamboo Fiber-Reinforced Epoxy Hybrid Composites for Semistructural Applications: Fabrication and Characterization. *Biomass Convers. Biorefin.* **2024**, *14* (15), 17761−17777.
(16) Li, L.; Yan, Y.; Liang, J.; Zhao, J.; Lyu, C.; Zhai, H.; Wu, X.; Wang, G. Wearable EMI Shielding Composite Films with Integrated Optimization of Electrical Safety, Biosafety and Thermal Safety. *Adv. Sci.* **2024**, *11* (21), 2400887.
(17) Fang, C.; Yang, R.; Zhang, Z.; Zhou, X.; Lei, W.; Cheng, Y.; Zhang, W.; Wang, D. Effect of Multi-Walled Carbon Nanotubes on the Physical Properties and Crystallisation of Recycled PET/TPU Composites. *RSC Adv.* **2018**, *8* (16), 8920−8928.
(18) Shi, Y.; Wu, S.; Chen, J.; Tang, L.; Gao, J.; Zou, H.; Song, P.; Qiu, T. Hierarchically Building Flame Retardant and Flexible Electromagnetic Interference Shielding Composites with Tunable Mechanism. *J. Mater. Sci. Technol.* **2025**, *239*, 39−54.
(19) Li, J.; Gao, J.; Wang, X.; Guo, Y.; Cheng, F. Spinel Ferrite Transformation for an Efficient Fe Removal from Circulating Fluidized Bed Fly Ash by Carbothermal Reduction at a Low Temperature. *ACS Omega* **2022**, *7* (22), 18612−18622.
(20) Jun, Y. S.; Habibpour, S.; Hamidinejad, M.; Park, M. G.; Ahn, W.; Yu, A.; Park, C. B. Enhanced Electrical and Mechanical Properties of Graphene Nano-Ribbon/Thermoplastic Polyurethane Composites. *Carbon* **2021**, *174*, 305−316.
(21) Xie, Y.; Zhu, J.; Fu, L.; Yang, W.; Li, D.; Zhou, L. TPU with Outstanding Wettability and Hydrophilic Stability Is Obtained by Plasma-Induced Graft Polymerization. *Appl. Surf. Sci.* **2024**, *654*, 159509.
(22) Zhong, Y.; Guo, Y.; Li, M.; Wei, X.; Wang, J. A Hollow Hybrid Separated Structure Based on Ni/Pani-Fe_3O_4 Constructed for an Ultra-Efficient Electromagnetic Interference Shielding and Hydrophobic PPTA Fabric. *J. Alloys Compd.* **2022**, *925*, 166666.
(23) Wang, H.; Chen, K.; Shi, Y.; Zhu, Y.; Jiang, S.; Liu, Y.; Wu, S.; Nie, C.; Fu, L.; Feng, Y.; Song, P. Flame Retardant and Multifunctional BC/MXene/MSiCnw/FRTPU Aerogel Composites with Superior Electromagnetic Interference Shielding via "Consolidating" Method. *Chem. Eng. J.* **2023**, *474*, 145904.
(24) Praveen, M.; Karthikeya, G. S.; Krishna, R. H.; Mamatha, G. M.; Manjunatha, C.; Khosla, A.; Nagabhushana, B. M. The Role of Magnetic Nano $CoFe_2O_4$ and Conductive MWCNT/Graphene in LDPE-Based Composites for Electromagnetic Interference Shielding in X-Band. *Diam. Relat. Mater.* **2022**, *130*, 109501.
(25) Simon, R. M. Emi Shielding Through Conductive Plastics. *Polym. Plast. Technol. Eng.* **1981**, *17* (1), 1−10.
(26) Fang, X.; Sun, H.; Wu, C.; Fang, Z.; Li, M.; Zhao, L.; Tian, B.; Verma, P.; Wang, J.; Maeda, R.; Jiang, Z. Ag Nanoparticle-Thiolated Chitosan Composite Coating Reinforced by Ag-S Covalent Bonds with Excellent Electromagnetic Interference Shielding and Joule Heating Performances. *ACS Appl. Mater. Interfaces* **2023**, *15* (23), 28465−28475.
(27) Yun, T.; Kim, H.; Iqbal, A.; Cho, Y. S.; Lee, G. S.; Kim, M.-K.; Kim, S. J.; Kim, D.; Gogotsi, Y.; Kim, S. O.; et al. Electromagnetic Shielding of Monolayer MXene Assemblies. *Adv. Mater.* **2020**, *32* (9), 1906769.
(28) Gill, N.; Sharma, A. L.; Gupta, V.; Tomar, M.; Pandey, O. P.; Singh, D. P. Enhanced Microwave Absorption and Suppressed Reflection of Polypyrrole-Cobalt Ferrite-Graphene Nanocomposite in X-Band. *J. Alloys Compd.* **2019**, *797*, 1190−1197.
(29) Kaushal, A.; Singh, V. Melt-Processed Graphite-Polypropylene Composites for EMI Shielding Applications. *J. Electron. Mater.* **2020**, *49* (9), 5293−5301.
(30) Shi, Y.; Yao, A.; Han, J.; Wang, H.; Feng, Y.; Fu, L.; Yang, F.; Song, P. Architecting Fire Safe Hierarchical Polymer Nanocomposite Films with Excellent Electromagnetic Interference Shielding via Interface Engineering. *J. Colloid Interface Sci.* **2023**, *640*, 179−191.
(31) Ahmed, I.; Khan, A. N.; Jan, R.; Gul, I. H. Structure − Properties Relationships of Graphene and Spinel Nickel Ferrites Based Poly(Vinylidene Fluoride) Hybrid Polymer Nanocomposites for Improved Dielectric and EMI Shielding Characteristics. *Mater. Res. Bull.* **2022**, *148*, 111687.
(32) Liu, M.; Chen, K.; Shi, Y.; Wang, H.; Wu, S.; Huang, R.; Feng, Y.; Tang, L.; Liu, X.; Song, P. High-Performance Flexible Nanocomposites with Superior Fire Safety and Ultra-Efficient Electromagnetic Interference Shielding. *J. Mater. Sci. Technol.* **2023**, *166*, 133−144.
(33) Liu, M.; Wu, S.; Huang, R.; Shi, Y.; Wang, H.; Feng, Y.; Tang, L.; Gao, J.; Song, P.; Lai, Y. Construction of Mechanically Robust and Fire Safe Thermoplastic Polyurethane-Based Nanocomposites for Electromagnetic Interference Shielding. *Compos. Part A Appl. Sci. Manuf.* **2023**, *175*, 107818.
(34) Liu, M.; Chen, K.; Shi, Y.; Wu, S.; Feng, Y.; Fu, L.; Gao, J.; Tang, L.; Yang, F. Mechanically Strong Hierarchical Nanosystem for Fire Protection and Electromagnetic Interference Shielding. *Compos. B Eng.* **2023**, *261*, 110795.
(35) Chen, K.; Wang, H.; Shi, Y.; Liu, M.; Feng, Y.; Fu, L.; Song, P. Realizing Balanced Flame Retardancy and Electromagnetic Interference Shielding in Hierarchical Elastomer Nanocomposites. *J. Colloid Interface Sci.* **2024**, *653*, 634−642.
(36) Wang, C.; Guo, Y.; Chen, J.; Zhu, Y. Transparent and Flexible Electromagnetic Interference Shielding Film Based on Ag Nanowires/Ionic Liquids/Thermoplastic Polyurethane Ternary Composites. *Compos. Commun.* **2023**, *37*, 101444.
(37) Shui, X.; Chung, D. D. L. Nickel Filament Polymer-Matrix Composites with Low Surface Impedance and High Electromagnetic Interference Shielding Effectiveness. *J. Electron. Mater.* **1997**, *26* (8), 928−934.
(38) Shen, B.; Zhai, W.; Tao, M.; Ling, J.; Zheng, W. L. Multifunctional Polyetherimide/Graphene@Fe_3O_4 Composite Foams for Shielding of Electromagnetic Pollution. *ACS Appl. Mater. Interfaces* **2013**, *5* (21), 11383−11391.
(39) Chen, Y.; Zhang, H.-B.; Yang, Y.; Wang, M.; Cao, A.; Yu, Z.-Z. High-Performance Epoxy Nanocomposites Reinforced with Three-Dimensional Carbon Nanotube Sponge for Electromagnetic Interference Shielding. *Adv. Funct. Mater.* **2016**, *26* (3), 447−455.
(40) Govindasamy, T.; Mathew, N. K.; Asapu, V. K.; Subramanian, V.; Subramanian, B. Evaluating the Microwave Absorbing Performance of Polymer-Free Thin Fe_3O_4−MWCNT NCs in X-Band Region. *Surf. Interfaces* **2024**, *44*, 103716.
(41) Lozitsky, O. V.; Vovchenko, L. L.; Matzui, L. Y.; Oliynyk, V. V.; Zagorodnii, V. V. Microwave Properties of Epoxy Composites with Mixed Filler Carbon Nanotubes/$BaTiO_3$. *Appl. Nanosci.* **2020**, *10* (8), 2759−2767.
(42) Zhang, Z.; Chen, X.; Wang, Z.; Heng, L.; Wang, S.; Tang, Z.; Zou, A. Y. Carbonyl Iron/Graphite Microspheres with Good Impedance Matching for Ultra-Broadband and Highly Efficient Electromagnetic Absorption. *Opt. Mater. Express* **2018**, *8* (11), 3319−3331.
(43) Li, Y.; Huang, X.; Hu, Z.; Jiang, P.; Li, S.; Tanaka, T. Large Dielectric Constant and High Thermal Conductivity in Poly(Vinylidene Fluoride)/Barium Titanate/Silicon Carbide Three-Phase Nanocomposites. *ACS Appl. Mater. Interfaces* **2011**, *3* (11), 4396−4403.
(44) Kumar, P.; Negi, P.; Dixit, A. K.; Baskey, H. B.; Kumar, S.; Mishra, A. K.; Kumar, A. Superparamagnetic Nanocubes of Co and Cu Co-Doped Mn-Based Ferrites as Microwave Absorbing Material. *Mater. Chem. Phys.* **2024**, *319*, 129360.
(45) Ruchi; Gupta, V.; Dalal, R.; Goyal, S. L. Electromagnetic Interference Shielding Performance of In-Situ Polymerized PANI/Fe_3O_4 Nanocomposites in X-Band Frequency Range. *Polym. Bull.* **2024**, *81* (6), 5155−5178.
(46) Ucpinar Durmaz, B.; Salman, A. O.; Aytac, A. Electromagnetic Interference Shielding Performances of Carbon-Fiber-Reinforced

https://doi.org/10.1021/acsanm.5c04619
ACS Appl. Nano Mater. 2026, 9, 353−369

PA11/PLA Composites in the X-Band Frequency Range. *ACS Omega* **2023**, *8* (25), 22762−22773.
(47) Saha, S.; Chakraborty, T.; Saha, A.; Das, S.; Pramanik, G.; Pradhan, A. K.; Chakraborty, C.; Das, S.; Sutradhar, S. A Multi-Layer Design of Hexaferrite Decorated Graphene Derivatives Incorporated PVDF Nanocomposite Films; Understanding the Role of GO/RGO for Outstanding Electromagnetic Wave Absorption at Microwave Frequencies. *Carbon* **2024**, *220*, 118829.
(48) Lu, W.; Zhou, Y.; Xu, H. Dual-Gradient MXene/AgNWs/Hollow-Fe_3O_4/CNF Composite Films for Thermal Management and Electromagnetic Shielding Applications. *Compos. Commun.* **2024**, *51*, 102077.
(49) Liu, L.; Bian, X. M.; Hou, Z. L.; Wang, C. Y.; Li, Z. S.; Hu, H. D.; Qi, X.; Zhang, X. Electromagnetic Response of Magnetic Graphene Hybrid Fillers and Their Evolutionary Behaviors. *J. Mater. Sci.: Mater. Electron.* **2016**, *27* (3), 2760−2772.
(50) Wang, H.; Jiang, Y.; Ma, Z.; Shi, Y.; Zhu, Y.; Huang, R.; Feng, Y.; Wang, Z.; Hong, M.; Gao, J.; et al. Hyperelastic, Robust, Fire-Safe Multifunctional MXene Aerogels with Unprecedented Electromagnetic Interference Shielding Efficiency. *Adv. Funct. Mater.* **2023**, *33* (49), 2306884.
(51) Ren, F.; Song, D.; Li, Z.; Jia, L.; Zhao, Y.; Yan, D.; Ren, P. Synergistic Effect of Graphene Nanosheets and Carbonyl Iron−Nickel Alloy Hybrid Filler on Electromagnetic Interference Shielding and Thermal Conductivity of Cyanate Ester Composites. *J. Mater. Chem. C Mater.* **2018**, *6* (6), 1476−1486.
(52) Mudasar, M.; Zh, X. U.; Sy, L.; Li, X.; Cheng, X. Tailoring Permittivity and Permeability of M-Type Hexagonal Ferrite and 2D $Ti_3C_2T_x$ MXene Composites for Broadband Microwave Stealth Performance. *Mater. Chem. Phys.* **2024**, *315*, 129031.
(53) Ali, K. S. A.; Ravikumar, M. M.; Mohammed, J.; Farouk, N.; Mohanavel, V.; Ravichandran, M. Investigation of Ku Band Microwave Absorption of Three-Layer $BaFe_{12}O_{19}$, Carbon-Fiber@Fe_3O_4, and Graphene@$BaFe_{12}O_{19}$@Fe_3O_4 Composite. *J. Alloys Compd.* **2021**, *884*, 161045.
(54) Xu, L.; Si, R.; Ni, Q.; Chen, J.; Zhang, J.; Ni, Q. Q. Synergistic Magnetic/Dielectric Loss and Layered Structural Design of Ni@carbon Fiber/Ag@graphene Fiber/Polydimethylsiloxane Composite for High-Absorption EMI Shielding. *Carbon* **2024**, *225*, 119155.
(55) Ji, D.; Wang, Y.; He, C.; Cui, K.; Han, P.; Sun, N.; Li, Y. High-Efficiency Electromagnetic Shielding Based on Multipolar Effect in RGO/MXene Aerogels Decorated with Ordered Fe_3O_4 Cluster. *Carbon* **2024**, *226*, 119189.
(56) Kumari, S.; Dalal, J.; Kumar, A.; Pal, R.; Chahal, R.; Ohlan, A. Enhanced Microwave Absorption Properties of Conducting Polymer@graphene Composite to Counteract Electromagnetic Radiation Pollution: Green EMI Shielding. *RSC Adv.* **2024**, *14* (1), 662−676.
(57) Huang, Y.; Zhang, Z.; Liang, Z.; Hu, Y.; Zhang, Q.; Zhang, P.; Xing, Y.; Wan, C. Ultra-Wideband Electromagnetic Interference Shielding Properties of Parallel Expanded Graphite/Fe_3O_4 Composites. *Int. J. Appl. Ceram. Technol.* **2024**, *21* (3), 2438−2447.
(58) Lu, M. M.; Cao, M. S.; Chen, Y. H.; Cao, W. Q.; Liu, J.; Shi, H. L.; Zhang, D. Q.; Wang, W. Z.; Yuan, J. Multiscale Assembly of Grape-Like Ferroferric Oxide and Carbon Nanotubes: A Smart Absorber Prototype Varying Temperature to Tune Intensities. *ACS Appl. Mater. Interfaces* **2015**, *7* (34), 19408−19415.
(59) Wang, Y.; Yao, L.; Zheng, Q.; Cao, M. S. Graphene-Wrapped Multiloculated Nickel Ferrite: A Highly Efficient Electromagnetic Attenuation Material for Microwave Absorbing and Green Shielding. *Nano Res.* **2022**, *15* (7), 6751−6760.
(60) Zhang, Y.; Wang, W.; Xie, J.; Dai, K.; Zhang, F.; Zheng, Q. Smart and Flexible CNTs@MXene Heterostructure-Decorated Cellulose Films with Excellent Electrothermal/Photothermal Conversion and EMI Shielding Performances. *Carbon* **2022**, *200*, 491−499.
(61) Guo, D.; Mu, C.; Liu, Q.; Wang, B.; Xiang, J.; Nie, A.; Zhai, K.; Shu, Y.; Xue, T.; Wen, F.; Liu, Z. Aramid Nanofiber/Polypyrrole Composite Films for Broadband EMI Shielding, Wearable Electronics, Joule Heating, and Photothermal Conversion. *ACS Appl. Nano Mater.* **2023**, *6* (16), 15108−15118.
(62) Wang, L.; Lang, L.; Hu, X.; Gao, T.; He, M.; Qiu, H.; Ji, X.; Guo, H.; Zhang, Y.; Huang, S. Multifunctional Ionic Bonding-Strengthened ($Ti_3C_2T_x$ MXene/CNF)-(BNNS/CNF) Composite Films with Janus Structure for Outstanding Electromagnetic Interference Shielding and Thermal Management. *J. Mater. Sci. Technol.* **2025**, *224*, 46−55.
(63) Dai, M.; Zhou, D.; Ren, H.; Deng, S.; Jiang, Y.; Sun, J.; Shi, S.; Chen, J.; Cheng, F.; Li, X. Cellulose-Based Multifunctional Film for Electromagnetic Interference Shielding, Joule Heating, and Flame Retardancy. *Diam. Relat. Mater.* **2024**, *143*, 110883.
(64) Liu, M.; Zhang, H.; Zhang, Z.; Zhang, K.; Chen, Z.; Pan, L.; Zhou, J. Jujube-Cake Inspired Lightweight and Flexible MXene/Liquid Metal/Bacterial Cellulose Electromagnetic Interference Shielding Film with Excellent Joule Heating and Thermal Conductivity. *Compos. Sci. Technol.* **2024**, *255*, 110722.
(65) Wei, H.; Lei, T.; Ma, L.; Li, W. Aramid Nanofiber-Reinforced Carbon Nanotubes@cobalt Ferrite Nanoparticles Aerogel Films Achieve Excellent Electromagnetic Interference Shielding, Photothermal and Joule Heating Performance. *Ceram. Int.* **2024**, *50*, 50388−50396.
(66) Ren, D.; Zhao, C.; Zhang, S.; Zhang, K.; Huang, F. Novel Sulfur-Containing Carbon Nanotubes with Graphene Nanoflaps for Stretchable Sensing, Joule Heating, and Electro-Thermal Actuating. *Adv. Funct. Mater.* **2023**, *33* (21), 2300517.
(67) Wang, L.; Li, G.; Chen, C.; Zhang, H.; Fang, L.; Wang, Z.; Tu, X.; Wang, Z.; Wang, P.; He, W. Polystyrene-Polyisoprene-Polystyrene Coated Fe_3C−C/MXene Composite Film Based Flexible, and Multifunctional Patch for Electromagnetic Interference Shielding and Joule Heating. *Carbon* **2024**, *228*, 119386.
(68) Guo, Z.; Zhao, Y.; Luo, P.; Chen, Z.; Song, P.; Jin, Y.; Pei, L.; Ren, F.; Ren, P. Durable and Sustainable $CoFe_2O_4$@MXene-Silver Nanowires/Cellulose Nanofibers Composite Films with Controllable Electric−Magnetic Gradient towards High-Efficiency Electromagnetic Interference Shielding and Joule Heating Capacity. *Chem. Eng. J.* **2024**, *485*, 149691.
(69) Guo, Z.; Ren, P.; Wang, J.; Tang, J.; Zhang, F.; Zong, Z.; Chen, Z.; Jin, Y.; Ren, F. Multifunctional Sandwich-Structured Magnetic-Electric Composite Films with Joule Heating Capacities toward Absorption-Dominant Electromagnetic Interference Shielding. *Compos. B Eng.* **2022**, *236*, 109836.

https://doi.org/10.1021/acsanm.5c04619
ACS Appl. Nano Mater. 2026, 9, 353−369